THE ASTROPHYSICAL JOURNAL, 396:201–218, 1992 September 1

X-RAY VARIABILITY OF SCORPIUS X-1 DURING A MULTIWAVELENGTH CAMPAIGN

P. HERTZ,[1] B. VAUGHAN,[2,3] K. S. WOOD,[1] J. P. NORRIS,[4] K. MITSUDA,[5] P. F. MICHELSON,[2] AND T. DOTANI[5]

Received 1991 December 30; accepted 1992 March 9

ABSTRACT

Scorpius X-1 was observed with the Japanese X-ray satellite *Ginga* on 1989 March 9–11 as part of a multiwavelength campaign. The source was observed to be on the flaring branch for the first 31 hr, on the lower normal branch for the next 7 hr, and on the flaring branch during a brief observation 17 hr after the final normal branch observation.

We constructed a standard color-color, or Z-, diagram for Sco X-1. We then parameterized the state of Sco X-1 by determining s_Z, the distance along the Z-diagram from the flaring branch–normal branch vertex, as a function of time. Sco X-1 moved smoothly and continuously through the Z-diagram and was never observed to jump from one branch to another. All observed spectral characteristics (intensity, X-ray hardness ratios) are well correlated with s_Z, indicating that the source changes its physical state smoothly as it moves along the Z-diagram. The tight correlation of observables with s_Z is consistent with variation of a single physical parameter being responsible for the changes in state. There is no correlation between $\dot{s}_Z$, the rate of change of s_Z, and observed spectral characteristics indicating that there is little, if any, hysteresis or memory in the spectral state of Sco X-1 and that motion in the Z-diagram is essentially stochastic. The range of observed values of $\dot{s}_Z$ depends on s_Z: s_Z always changes slowly along the flaring branch when it is near the flaring branch–normal branch vertex, but can change rapidly during the excursions up and down the flaring branch which correspond to large flares. A self-similarity is observed in the temporal profile of flares which is independent of flare amplitude.

The temporal characteristics observed—including quasi-periodic oscillations, high-frequency noise, and very low frequency noise—are consistent with previous observations of Sco X-1. Quasi-periodic oscillations are observed on both the normal branch (6.3 Hz mean frequency) and the lower flaring branch (14.4 Hz mean frequency), but not on the upper flaring branch. Limits are placed on the fractional rms variation of quasi-periodic oscillations on the upper flaring branch of $\lesssim 2\%$ of the total intensity. The characteristics of the observed red noise components are found to vary along the flaring branch. The fractional rms variation of very low frequency noise increases from $\lesssim 2\%$ to $\gtrsim 6\%$ as Sco X-1 moves from the flaring branch–normal branch vertex to the upper end of the flaring branch; the power-law index for very low frequency noise, α, remains constant along the flaring branch ($\alpha = 1.72 \pm 0.01$). Both the rms fractional variation and the width of the high-frequency noise component vary as Sco X-1 moves out the flaring branch, with the rms fractional variation decreasing from $\sim 3\%$ to $\lesssim 1\%$ and the Gaussian rms width decreasing from ~ 15 Hz to ~ 5 Hz. No dependence on $\dot{s}_Z$ is observed for any of the temporal characteristics.

A search for coherent pulsations was made in both high time resolution optical and X-ray data. Limits on the 95% confidence limit pulsed amplitude are set at 0.10% (optical) and 0.19% (X-ray) for $\nu < 50$ Hz and 0.26% (X-ray) for $\nu < 400$ Hz. A search was made for optical quasi-periodic oscillations in data obtained while normal branch oscillations were observed in the *Ginga* data; none were seen with an upper limit to the fractional rms variation of 0.23% of the total intensity.

Subject headings: binaries: close — stars: individual (Scorpius X-1) — stars: variables: other — X-rays: stars

1. INTRODUCTION

Scorpius X-1 is the brightest extrasolar X-ray source in the sky and the historical prototype of the class of low-mass X-ray binaries (LMXBs). LMXBs contain a neutron star accreting matter from a close, low-mass, main-sequence binary companion through Roche lobe overflow (Lewin & Joss 1983; White 1989). In recent years, our understanding of LMXBs has been considerably enhanced by the closely coupled discoveries of quasi-periodic oscillations (QPOs) and distinct spectral states in LMXBs. Sco X-1 is one of six LMXBs which have been observed to have up to three spectral states or branches; each branch has its own spectrum, characteristic QPO and red noise phenomena, and variability properties. When an X-ray color-color diagram is made of these six sources, it is found that the X-ray colors, or hardness ratios, are correlated in all three spectral states in such a way that the loci of the source states form a doubly bent line which looks somewhat like a "Z" (Hasinger 1987; Hasinger & van der Klis 1989). These six sources (Sco X-1, GX340+0, GX349+2, GX5−1, GX17+2, Cyg X-2) are known as Z-sources, and the three legs of the "Z" are the horizontal branch, the normal branch, and the flaring branch (see Lewin, van Paradijs, & van der Klis 1988 and van der Klis 1989a for reviews of QPO observations).

Sco X-1 has long been known to have bimodal spectral behavior. Until recently these spectral states were termed the

[1] E. O. Hulburt Center for Space Research, Code 4121, Naval Research Laboratory, Washington, DC 20375-5000.
[2] Department of Physics, Stanford University, Stanford, CA 94305.
[3] Astronomical Institut "Anton Pannekoek," University of Amsterdam, Roetersstraat 15, 1018 WB Amsterdam, The Netherlands.
[4] Laboratory for High Energy Astrophysics, Code 668, NASA Goddard Space Flight Center, Greenbelt, MD 20771.
[5] Institute for Space and Astronautical Science, 3-1-1 Yoshinodai, Sagimahara, Kanagawa 229, Japan.

"active" and "quiescent" states, and Sco X-1 was observed to remain in a given state for a few hours to a few days (Bradt et al. 1975; Canizares et al. 1975). The discovery of three spectral and QPO states in other LMXBs, including Cyg X-2 (Hasinger 1988b; Dotani & Mitsuda 1988) and GX17+2 (Langmeier 1988; Penninx et al. 1990), as well as the observation of a third spectral state in Sco X-1 (Hasinger, Priedhorsky, & Middleditch 1989), led to the identification of the "active" state with the flaring branch and the "quiescent" state with the normal branch (Hasinger 1987), while the third state seen by Hasinger et al. (1989) is identified by the presence of low-frequency noise as the only observation to date of Sco X-1 on the horizontal branch.

Because it is so bright, Sco X-1's spectra and QPO behavior has been well studied. On the normal branch, where spectral hardness is strongly correlated with intensity, Sco X-1 exhibits a QPO with mean frequency $\sim$6 Hz, FWHM $\sim$1 Hz, and fractional rms variation $\sim$5% of total intensity (Middleditch & Priedhorsky 1986; Priedhorsky et al 1986; van der Klis et al. 1987; Hasinger & van der Klis 1989). This normal-branch QPO is observed only on the lower normal branch near the flaring branch and has never been observed on the upper normal branch near the horizontal branch (Hasinger et al. 1989). The frequency and fractional rms variation of the 6 Hz normal branch QPO usually vary by $\sim$10% and are weakly anticorrelated with source intensity ($\nu \propto I^{-0.5}$; Middleditch & Priedhorsky 1986; van der Klis et al. 1987). The flaring branch is characterized by flares of 25%–100% in intensity lasting tens of minutes, interspersed with quiescent behavior. Spectral hardness is strongly correlated with intensity during flares. On the lower flaring branch, close to the flaring branch–normal branch vertex, 10–20 Hz QPO with fractional rms variation between 5% and 10% of intensity are observed, with the QPO frequency strongly correlated with source intensity ($\nu \propto I^3$; Priedhorsky et al. 1986; van der Klis et al. 1987). The horizontal branch is recognized by a constant spectral hardness, independent of changes in source intensity. On the single occasion Sco X-1 was observed on the horizontal branch, no QPOs were observed (Hasinger et al. 1989).

In addition to QPOs, several red noise components are seen in Sco X-1 power spectra. On the flaring and normal branches, a steep red noise component, which is identified with the very low frequency noise (VLFN) seen in GX5−1 and Cyg X-2, is observed below 1 Hz. The VLFN has a power-law index between −1.4 and −2 and fractional rms variation ranging from $\sim$1.5% of intensity on the normal branch to $\sim$6% of intensity on the upper flaring branch (van der Klis et al. 1987; Hasinger et al. 1989; Hasinger & van der Klis 1989). Low-frequency noise (LFN), similar to that observed in Cyg X-2 and GX5−1, has been observed in Sco X-1 only when it is on the horizontal branch; the presence of LFN is one of the key observational features of horizontal branch behavior. The LFN in Sco X-1 can be described as a broad peak centered at $\sim$2 Hz or as a power law with slope $\sim$1 and exponential cutoff between 2 and 5 Hz (Hasinger et al. 1989; Hasinger & van der Klis 1989). Excess power with a high-frequency cutoff of $\sim$60 Hz is seen on all spectral branches (Middleditch & Priedhorsky 1986; Hasinger et al. 1989) and is referred to as high-frequency noise (HFN) (Hasinger & van der Klis 1989).

Sco X-1 is not only the brightest celestial X-ray source, it is also a relatively bright radio, optical, and ultraviolet source. It was the target of numerous multiwavelength campaigns in the 1970s prior to the identification of spectral states with high-frequency temporal behavior (e.g., Canizares et al. 1973; Bradt et al. 1975; Canizares et al. 1975; Mook et al. 1975; Ilovaisky et al. 1980; Willis et al. 1980; Petro et al. 1981; see also Miyamoto & Matsuoka 1977; Mason 1988). Our March 1989 observation of Sco X-1 with the Japanese X-ray satellite *Ginga* was the basis of a multiwavelength campaign specifically to study the different aspects of Sco X-1's behavior as a function of spectral branch. In addition, we hoped to use the large area of *Ginga* and its high time resolution mode to detect the underlying, possibly millisecond, spin period of Sco X-1's neutron star primary.

During the *Ginga* observations reported here, Sco X-1 was usually on the flaring branch. However, on the second day Sco X-1 moved onto the normal branch for several hours of observations. We have concentrated on characterizing the observable properties of Sco X-1 as a function of its spectral state. In particular we parameterize the spectral state of Sco X-1 with a single parameters, s_Z, which is defined in § 4. Because of the large number of flaring branch observations, we are particularly sensitive to dependencies while on that branch.

In this paper we summarize the principal aspects of the multiwavelength campaign (§ 2). Preliminary results based on these *Ginga* observations of Sco X-1, some of which are superseded by this paper, have been reported by Wood et al. (1989a, b) and Hertz et al. (1990b, 1992). We then present the X-ray observations (§ 3) and the color-color and color-magnitude diagrams (§ 4). It is here that we define s_Z and determine the spectral state of Sco X-1 for correlation with observations at other wavelengths; radio, optical, and ultraviolet observations and correlations are presented elsewhere (Hjellming et al. 1990b; Augesteijn et al 1992; Vrtilek et al. 1991), as are analyses of hard X-ray observations obtained with instruments aboard the Soviet space station Mir (Maisack et al. 1992; Pan et al. 1992). The results of our studies of quasi-periodic oscillations, millisecond pulsations, and HFN and VLFN are given in § 5 and § 6. We conclude by briefly relating these new observations to current models of Z-sources (§ 7).

2. THE MULTIWAVELENGTH CAMPAIGN

An observation of Sco X-1 with the Japanese X-ray satellite *Ginga* was conducted on 1989 March 9–11. The goals of the X-ray observation included (i) the study of QPOs with high photon count rates, including short time scale fluctuations, time lags, and correlations with gross spectral properties, (ii) a search for millisecond X-ray pulsations using coherence recovery techniques to account for binary motion of the source, and (iii) a search for signatures of nonaxisymmetric, gravitational radiation-induced, neutron star instability.

Subsequently, ground-based and space-based observations covering the electromagnetic spectrum from radio to hard X-rays were scheduled in order to search for correlations of non–X-ray properties with the X-ray spectral state of Sco X-1. Previous multiwavelength campaigns to observe Cyg X-2 and GX17+2 showed strong spectral state–dependent behavior in radio (Penninx et al. 1988; Hjellming et al. 1990), optical (van Paradijs et al. 1990), and ultraviolet (Vrtilek et al. 1990) observations. The results of the Sco X-1 multiwavelength campaign are consistent with previously observed behavior in Z-sources (Hjellming et al. 1990b; Augesteijn et al. 1992; Vrtilek et al. 1991).

Radio coverage was provided around the clock by the Very Large Array, the Australian Telescope, and the Westerbork

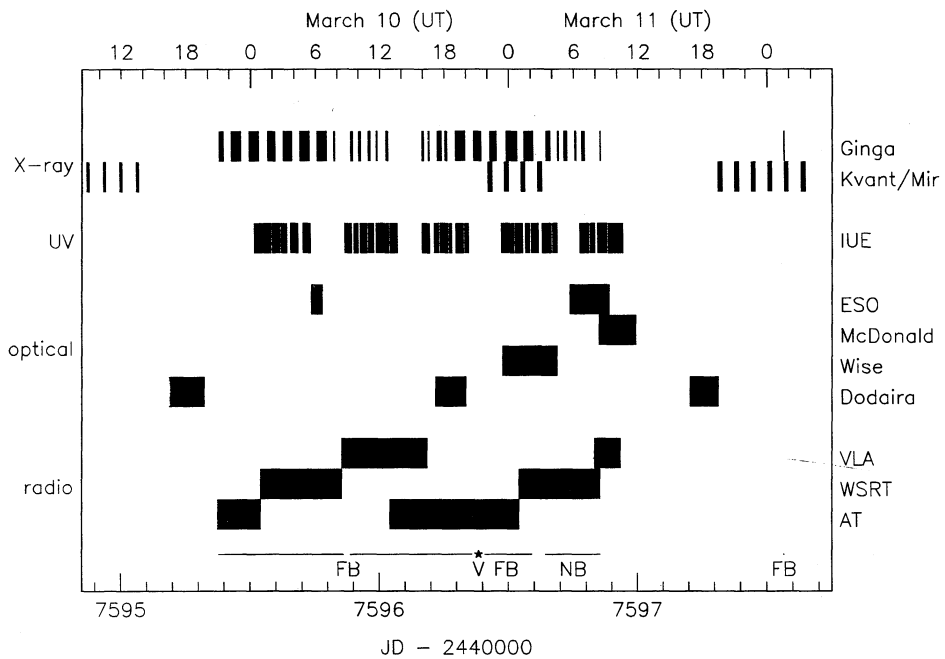

FIG. 1.—Timeline for the Sco X-1 multiwavelength campaign showing observing windows by instrument. For *Ginga* and Kvant/Mir, the gaps in the observations are due to occultations of Sco X-1 by the Earth. For *IUE*, individual exposures are indicated. For ground-based observatories, the hours during which data were collected are indicated. The last line in the figure indicates the times that Sco X-1 was observed on the flaring branch (FB), normal branch (NB), and near the flaring branch–normal branch vertex (V).

Radio Synthesis Telescope. Optical observations were scheduled at the European Southern Observatory, McDonald Observatory, Wise Observatory, and Dodaira Observatory. Although nearly continuous coverage was planned, worldwide clouds on March 10 reduced the optical coverage considerably. Continuous ultraviolet observations were conducted over a 40 hr period from both the European and American ground stations of the *International Ultraviolet Explorer*. Simulataneous hard X-ray observations were made with the Kvant astrophysics module aboard the Soviet space station Mir.

In Figure 1 we give an approximate timeline for the campaign. The coverage for each instrument in the campaign is shown. In Table 1 we give the types of data in the campaign data base, including the principal observers and primary observations made from each observatory during the campaign.

3. THE X-RAY OBSERVATIONS

The *Ginga* observations were made with the Large Area Counter (LAC), an array of eight multicell proportional counters with a total effective area of 4000 cm^2 (Makino 1987; Turner et al. 1989). The observations were performed using two different on-board data reduction modes, three different

TABLE 1

SCORPIUS X-1 MULTIWAVELENGTH CAMPAIGN

Observatory	Principal Observers	Character of Observations
Ginga	P. Hertz, K. Mitsuda, K. Wood	X-ray spectroscopy (1.5–19 keV, 12 channels, 250 ms time resolution); X-ray photometry (1–16 keV, 2 channels, 1 ms time resolution)
Kvant Module, *Mir* space station	G. Hasinger	Hard X-ray spectroscopy and photometry (20–200 keV, 25 ms time resolution)
International Ultraviolet Explorer	W. Penninx, S. Vrtilek	Ultraviolet spectroscopy (1200–2000 Å, 2000–3200 Å, 40 minute time resolution)
European Southern Observatory, Chile	T. Augusteijn, J. van Paradijs	90 cm telescope; optical multicolor photometry (Walraven *VBLUW*, 3250–6000 Å, 16 s time resolution)
McDonald Observatory, Texas	K. Horne, E. Robinson	90 cm telescope; optical photometry (unfiltered, 10 ms time resolution)
Dodaira Observatory, Japan	S. Kikuchi	91 cm telescope; optical multicolor photometry (8 bands, 3600–8800 Å, 23 s time resolution); optical polarimetry
Wise Observatory, Israel	N. Brosch, E. Leibowitz	1 m telescope; optical multicolor photometry (Johnson *UBVRI*, 3010–10200 Å, 2 minute time resolution); optical polarimetry
Very Large Array, New Mexico	R. Hjellming, W. Lewin	Radio multifrequency photometry (B-array, 1.49 GHz, 4.9 GHz, 8.4 GHz)
Australian Radio Telescope, Australia	R. Stewart, G. White	Radio photometry (8.7 GHz)
Westerbork Synthesis Radio Telescope, Netherlands	R. Strom	Radio photometry (333 MHz)

TABLE 2

DATA TYPES USED IN *Ginga* OBSERVATIONS OF SCORPIUS X-1

Data Type	Mode	Bit Rate	Detector Gain	Time Resolution (ms)	Spectral Channels	Energy Range (keV)	Integration Time (hr)	Plot Symbol
A	PC	High	Low	0.98	2	1.2–15.7	2.93	+
B	PC	Medium	Low	7.81	2	1.2–15.7	0.00	
C	MPC-3	High	High	7.81	12	1.5–18.7	0.19	○
D	MPC-3	Medium	High	62.50	12	1.5–18.7	5.73	×
E	MPC-3	Low	High	250.00	12	1.5–18.7	1.57	□
F	MPC-3	High	Low	7.81	12	1.2–36.8	1.78	△

telemetry bit rates, and two different detector gains; these combinations resulted in a total of six data types, each with different time and spectral resolution. We have labeled these as data types A–F (Table 2).

Data types A and B were obtained with the on-board computer in PC mode, the high time resolution photometry mode, and at low detector gain. In PC mode, there are two spectral channels available; for our observations, the energy ranges were set to 1.2–5.8 keV and 5.8–15.7 keV. When the LAC is operating in PC mode at high bit rate, the lower energy channel is read out every 1 ms, and the higher energy channel is read out every 2 ms (data type A). In PC mode at medium bit rate (data type B), the lower energy channel is read out every 8 ms and the higher energy channel is read out every 16 ms. We have not used any of the type B data in the study reported here because of a data overflow problem.

The MPC-3 mode of the *Ginga* on-board computer is for high time resolution spectroscopy. In this mode, the X-ray data are divided into 12 energy channels, and the channel break points depend on the detector gain. At high gain the energy range is 1.5–18.7 keV (data types C, D, and E), and at low gain the energy range is 1.2–36.8 keV (data type F). The time resolution of the data depends on the bit rate: 8 ms at high bit rate (data types C and F), 63 ms at medium bit rate (data type D), and 250 ms at low bit rate (data type E). The data types, properties, and observing time for each are summarized in Table 2.

Throughout this paper, wherever we plot data from different data types, we use the set of plotting symbols given in the final column of Table 2. In this manner, any systematic differences between data types become clear.

We present the X-ray light curve for Sco X-1 obtained during the campaign in Figure 2. The X-ray intensity plotted is the corrected count rate in the 2.3–18.7 keV energy band. In order to determine this quantity, the observed count rate must be corrected for the collimator response and for detector dead

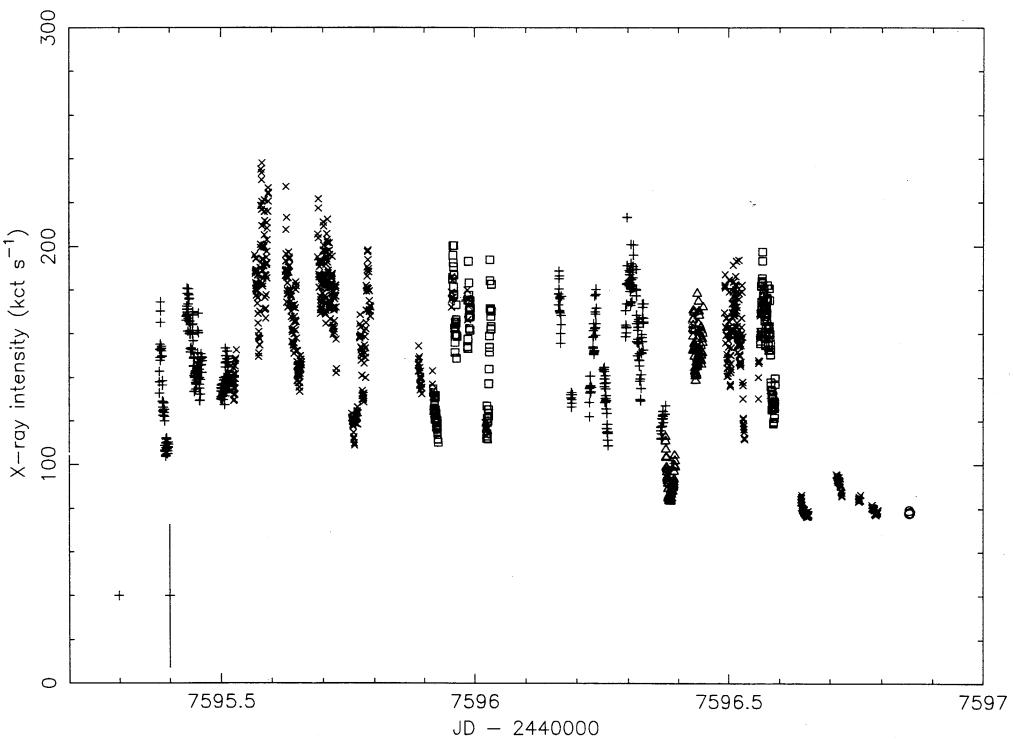

FIG. 2.—Light curve for Sco X-1 during the campaign. The intensity is the 2.3–18.7 keV corrected count rate. The plotting symbols represent the various data types; a key is in Table 2. The large gaps in the light curve represent Earth occultations of Sco X-1 during each *Ginga* orbit. Typical 1 σ uncertainties are shown in the lower left corner. The large error bar shows the uncertainty due to the aspect jitter and pointing uncertainties of *Ginga* and the small error bar shows the statistical uncertainty due to finite counting statistics.

TABLE 3

X-RAY COUNT RATES AND CORRECTIONS[a]

Time (JD')[b]	*Ginga* Orbit	Data Type	Detector Count Rate (kct s^{-1})	Dead Time Correction	Aspect Correction	Corrected Count Rate[c] (kct s^{-1})
5.380–5.398.....	1	A	17.9	0.75[d]	9.52[e]	128
5.433–5.464.....	2	A	21.3	0.75[d]	9.52[e]	152
5.500–5.516.....	3	A	21.0	0.75[d]	8.70[e]	137
5.517–5.523.....	3	C	12.1	1.53	7.55[e]	140
5.525–5.531.....	3	D	11.8	1.52	7.81	140
5.567–5.595.....	4	D	13.1	1.61	9.10	191
5.627–5.660.....	5	D	12.6	1.58	8.47	167
5.691–5.728.....	6	D	12.9	1.59	8.96	183
5.758–5.795.....	7	D	10.8	1.46	9.37	149
5.889–5.919.....	9	D	10.1	1.41	9.82	140
5.919–5.929.....	9	E	9.2	1.36	9.82	123
5.955–5.987.....	10	D	11.6	1.49	10.26	177
5.957–5.993.....	10	E	11.3	1.48	10.26	172
6.022–6.024.....	11	D	8.5	1.33	10.41	117
6.024–6.034.....	11	E	10.0	1.40	10.41	146
6.165–6.192.....	13	A	15.2	0.75[d]	14.29[e]	163
6.226–6.262.....	14	A	13.4	0.75[d]	14.29[e]	144
6.296–6.332.....	15	A	14.6	0.75[d]	15.38[e]	169
6.365–6.374.....	16	A	9.7	0.75[d]	16.67[e]	121
6.375–6.394.....	16	F	6.1	1.18	12.69	91
6.428–6.449.....	17	F	9.1	1.32	12.83	155
6.492–6.532.....	18	D	8.2	1.31	14.66	159
6.559–6.563.....	19	D	8.7	1.33	13.20	153
6.563–6.593.....	19	E	8.9	1.34	13.20	157
6.643–6.660.....	20	D	5.1	1.17	13.46	79
6.714–6.725.....	21	D	4.9	1.16	16.11	91
6.756–6.794.....	22	D	4.3	1.14	16.56	80
6.854–6.856.....	23	C	3.8	1.12	18.58[e]	78
7.566–7.567.....	34	E	[f]			

[a] All quantities averaged over single *Ginga* orbits.
[b] JD' = JD − 2,447,590.
[c] The uncertainty in corrected count rate can be significant due to spacecraft jitter (see eq. [1]).
[d] Estimated dead time correction includes scale factor for converting between energy bands.
[e] Estimated aspect correction.
[f] Data not analyzed here (see Wood et al. 1989a).

time; the count rate is not corrected for detector or window efficiency. In addition, PC mode data (data type A) must be corrected for its different energy band (1.2–15.7 keV).

Sco X-1 is so bright that direct observations can damage the detector. To reduce the detector count rates to safe levels, Sco X-1 was observed at collimator response levels C between 5% and 15%. At these collimator response levels, the collimator response is essentially independent of incident photon energy (Turner et al. 1989). The observed count rates were still quite high ($\sim$4–13 kilocounts s^{-1}) and moderate detector dead time corrections were required (20%–60%). For data types D, E, and F, the data were corrected for both the collimator response and detector dead time. For data types A and C, the data were corrected for detector dead time, but the detailed collimator response corrections were not available. We estimated average collimator response corrections for the two short data type C observations by requiring the mean corrected count rate to agree with contiguous type D observations. Finally, because the PC mode data (data type A) covers a different energy band, we have scaled it so that the mean of the type A data agrees with the mean of the types D and F data which immediately follow it. We summarize in Table 3 the magnitudes of the various corrections made to the data. Note that the tabulated corrections multiply the detector count rate to yield the corrected count rate; in particular the aspect correction is $1/C$, the inverse of the collimator response.

The uncertainties in the corrected count rates must include both counting statistics and uncertainties in the aspect. The counting statistics can be calculated simply from the detector count rates. There are several aspect uncertainties and jitters. First there is a slow drift due to error in the estimation of the gyro drift rates; this was typically 0.°3 per day in 1989. Second there is a drift of approximately 0.°1 per *Ginga* orbit in the pointing direction due to the interaction of the magnetic coils, which control pointing, and the geomagnetic field. The effects of these drifts are canceled by the attitude determinations, which are obtained every 4 or 32 s with an accuracy of better than 0.°05. Finally the momentum wheels cause a small jitter around the pointing direction with small amplitude, less than 0.°01, and rapid time scale, $\sim$1 s.

The only aspect uncertainty which adds appreciably to the uncertainty in the collimator response corrections is the uncertainty in the aspect determination, $\psi_{\rm aspect} \simeq 0.°05$. This uncertainty changes with a time scale of 32 s or less. By averaging the $1° \times 2°$ FWHM rectangular collimator response of the *Ginga* LAC over all roll angles, we estimate that the fractional uncertainty in the collimator response C, and hence in the corrected count rate, due to aspect jitter is

$$(\sigma_C/C)_{\rm aspect} = 0.45\psi_{\rm aspect}/C \ . \quad (1)$$

For $\psi_{\rm aspect} = 0.°05$, $(\sigma_C/C)_{\rm aspect}$ is 2% on axis, but 17% at $C = 0.13$ and 42% at $C = 0.054$; these values bracket the colli-

mator response during the Sco X-1 observations. For X-ray colors and hardness ratios, which are ratios of count rates, the uncertainties in the collimator response cancel out.

Sco X-1 was observed for half of each *Ginga* orbit, or about 45 minutes out of every 90 minutes, for the 36 hr campaign. It is impossible to plot a continuous light curve of Sco X-1 with reasonable resolution because of the large and frequent gaps in the observation—this is why Figure 2 looks like a set of vertical stripes. In Figure 3 we plot a matrix of Sco X-1 light curves from independent *Ginga* orbits on identical scales, but we have removed the observational gaps caused by Earth occultation of Sco X-1. The beginning time T_0 for orbit n_{orb} is

$$T_0(n_{orb}) = \text{JD } 2{,}447{,}595.27854 + 0.06632 n_{orb} . \quad (2)$$

The predominant variability time scales for Sco X-1 during the observation are clearly visible in Figure 3. Since this variability takes much longer than the 32 s time scale for aspect determination, we can be sure that it represents variability in the source Sco X-1 and not in the *Ginga* aspect determination. During much of the observation, Sco X-1 is flaring from the 100 kilocounts s^{-1} level to the 200 kilocounts s^{-1} level on time scales of $\sim$10 minutes. However, during the latter part of orbit 16 and during orbits 20–23, Sco X-1 is fainter ($\sim$80 kilocounts s^{-1}) and is not flaring. The flaring activity is identified with the flaring branch and the fainter state is identified with the normal branch (see § 4).

4. SPECTRAL BRANCHES AND THE Z-DIAGRAM

4.1. *The Color-Color and Color-Magnitude Diagrams*

In order to determine which spectral branch Sco X-1 is on during the campaign, we have constructed both color-magnitude and color-color diagrams of the X-ray data. We define four energy bands for the 12 channel spectroscopic data (MPC-3 mode, data types C–F): 2.3–4.6 keV, 4.6–6.9 keV, 6.9–9.2 keV, and 9.2–18.7 keV. These correspond to channels 2, 3, 4, and 5–8 for the low-gain data (data type F) and to channels 3–4, 5–6, 7–8, and 9–12 for the high-gain data (data types C–E). We then construct three X-ray hardness ratios from these energy bands. The soft hardness ratio S_{HR} is the ratio of the 4.6–6.9 keV count rate to the 2.3–4.6 keV count rate, the hard hardness ratio H_{HR} is the ratio of the 9.2–18.7 keV count rate to the 6.9–9.2 keV count rate, and the overall or broad hardness ratio B_{HR} is the ratio of the 6.9–18.7 keV corrected count rate to the 2.3–6.9 keV corrected count rate.

In Figure 4 we show the X-ray color-magnitude diagram for the observation; we have plotted the overall X-ray hardness

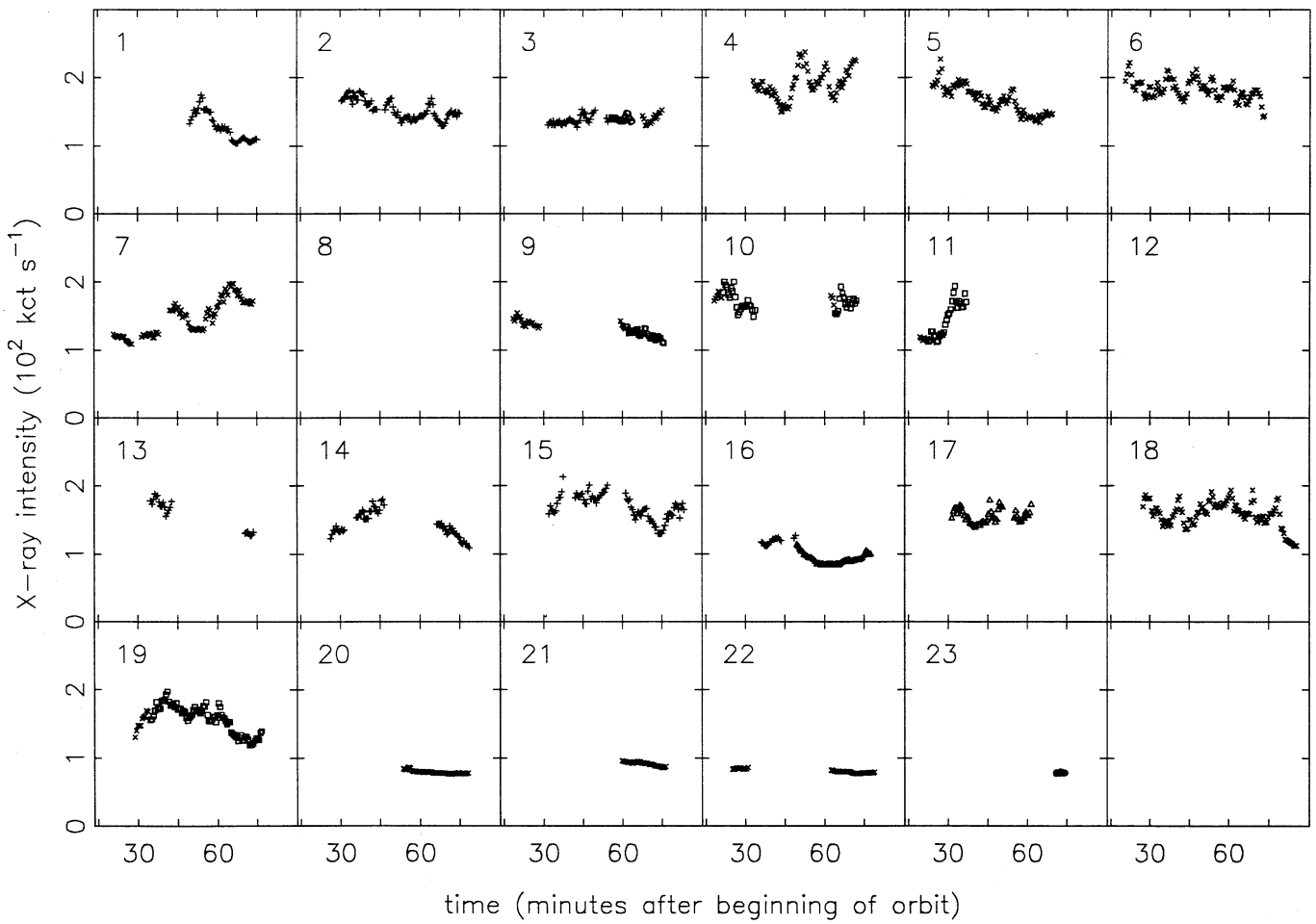

FIG. 3.—Light curves for Sco X-1 on a *Ginga* orbit-by-orbit basis. The plotting symbols represent the various data types; a key is in Table 2. The data shown here is the same shown in Fig. 2; here we show a separate light curve for each *Ginga* orbit. The scales are identical for each panel, and the orbit number is shown in the upper left corner of each panel. The exact times for each *Ginga* orbit are given in Table 3 and can be calculated from eq. (2).

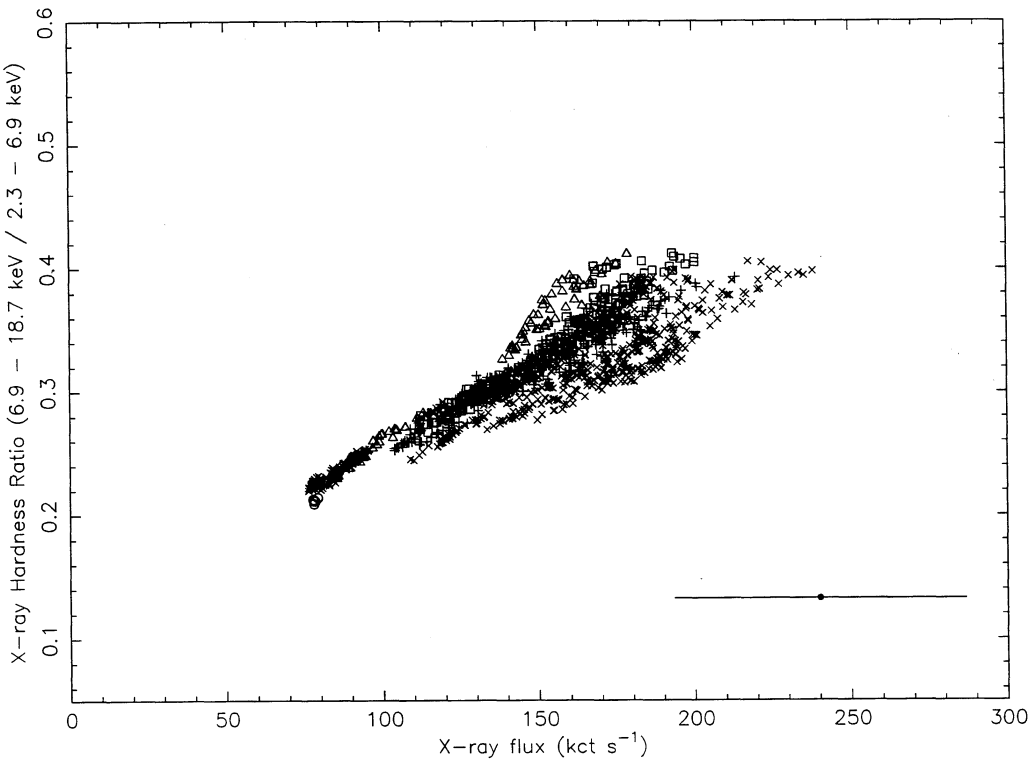

FIG. 4.—The X-ray color-intensity or color-magnitude diagram for Sco X-1 in which the broad hardness ratio B_{HR} is plotted against the corrected X-ray count rate. The data are binned in 32 s bins. The plotting symbols represent the various data types; a key is in Table 2. The spread in the diagram, which appears to depend on data type, actually depends on orbit number and can be entirely accounted for by uncertainties in the X-ray intensity due to aspect jitter and pointing uncertainty. A typical error bar, including aspect jitter, is shown in the lower right corner.

ratio B_{HR} against the X-ray intensity for data binned in 32 s accumulations. Only data types for which we have accurate aspect corrections are included (data types D–F). The uncertainties due to counting statistics are negligible in 32 s bins, typically 0.2% of the intensity of ± 0.001 for log(intensity). However, the uncertainties in the aspect correction are comparable to the jitter in the satellite pointing, which were $\sim 0.^{\circ}05$ during the Sco X-1 observation. As mentioned in § 3, this introduces uncertainty in the aspect correction between 17% and 42% for the Sco X-1 observations. In Figure 4 we show a typical uncertainty in the aspect correction for the intensity measurements. Note that the observations show a strong correlation between the broad hardness ratio and X-ray intensity, and that all of the spread in the color-magnitude diagram can be accounted for by the uncertainties in the aspect correction.

The correlation between the hardness ratio and the intensity indicates that Sco X-1 was on either the normal branch or the flaring branch during the observation. In order to resolve between the two, we have plotted the X-ray color-color diagram (Fig. 5) for the observation; here we can include all spectroscopic data (data types C–F) since the hardness ratios are independent of aspect corrections. The X-ray color-color diagram clearly shows that Sco X-1 was on the flaring branch for most of the observation, and on the lower normal branch for a small fraction of the observation. The X-ray color-color diagram in Figure 5 represents the lower half of a complete Z-diagram; the top half would consist of the horizontal branch and the upper normal branch (Hasinger & van der Klis 1989; Hasinger et al. 1989).

4.2. *The Z Diagram*

Hasinger (1987, 1988a) and Lamb (1989) have suggested that a single physical parameter changes as the source moves along the "Z"; they suggest that this parameter is the mass accretion rate $\dot{M}$. The tight correlation in both the X-ray color-magnitude diagram and the X-ray color-color diagram supports the single parameter hypothesis. In order to investigate whether all of the observables in our data are consistent with the single parameter hypothesis, we have defined a metric to measure the position of Sco X-1 along the "Z" at any time. We have chosen as the metric s_Z, the arc length along the "Z" from the flaring branch–normal branch vertex to the current position. The exact value of s_Z depends on both the energy channels chosen for the hardness ratios S_{HR} and H_{HR} and on the instrumental response of the *Ginga* LAC.

We define positive values of s_Z to be along the flaring branch, and negative values to be along the lower normal branch. To quantify s_Z, we fitted a rotated parabola to the color-color diagram shown in Figure 5. The best-fitted parabola is

$$S_{HR} \sin(\theta) + H_{HR} \cos(\theta) = a[S_{HR} \cos(\theta) - H_{HR} \sin(\theta)]^2 + b[S_{HR} \cos(\theta) - H_{HR} \sin(\theta)] + c\,, \quad (3)$$

where S_{HR} is the soft hardness ratio, H_{HR} is the hard hardness ratio, and

$$a = 43.59\,, \quad b = -5.49\,, \quad c = 0.97\,, \quad \theta = 36.^{\circ}07\,. \quad (4)$$

The vertex between the normal branch and the flaring branch

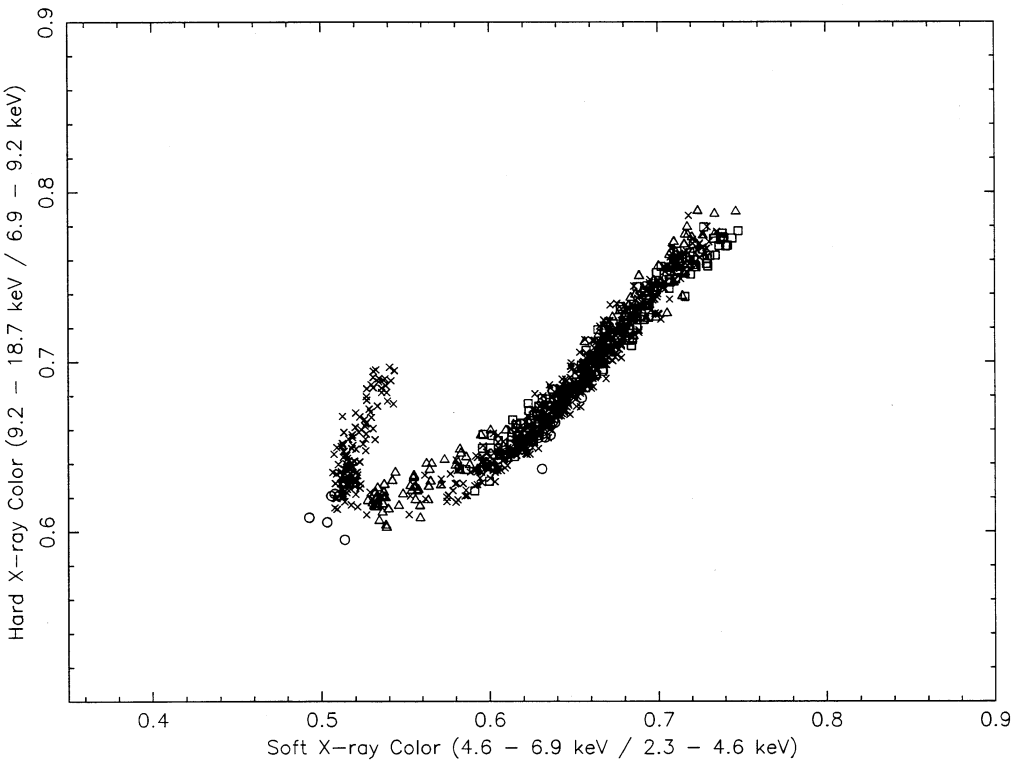

FIG. 5.—The X-ray color-color diagram or Z-diagram for Sco X-1 in which the hard hardness ratio H_{HR} is plotted against the soft hardness ratio S_{HR}. The data are binned in 32 s bins. The plotting symbols represent the various data types; a key is in Table 2. The right-hand branch is the flaring branch and the vertical branch is the lower half of the normal branch. A typical error bar is shown in the lower right corner.

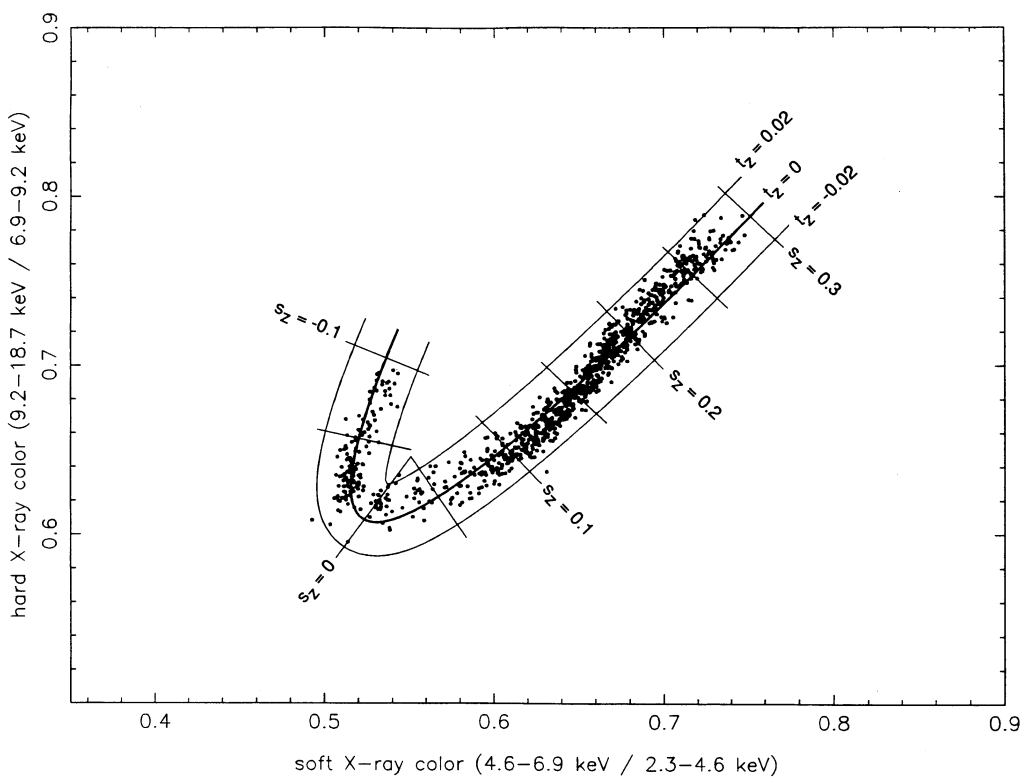

FIG. 6.—The Z-diagram of Sco X-1 from Fig. 5 is overlayed with the rotated parabola described by eqs. (3) and (4) along which s_Z is measured, as well as a grid showing the values of s_Z (distance along the Z-diagram measured from the flaring branch–normal branch vertex) and t_Z (distance from the center of the "Z" shaped curve).

has a soft hardness ratio $S_{HR} = 0.522$ and hard hardness ratio $H_{HR} = 0.609$.

For each two-color measurement in Figure 5 with coordinates S_{HR} and H_{HR}, we determine the point on the parabola closest to the measurement; let this point be designated $\mathscr{P}$. We then calculate s_Z as the arc length from the flaring branch–normal branch vertex to $\mathscr{P}$ along the parabola; we also determine how far the measurement is from the parabola by calculating t_Z, the linear distance from the measurement to $\mathscr{P}$. In Figure 6 we show the parabola described in equations (3) and (4), as well as s_Z and t_Z grid lines, superposed on the color-color diagram of Figure 5.

In Figure 7 we show various observational characteristics of Sco X-1 (X-ray intensity, soft hardness ratio S_{HR}, hard hardness ratio H_{HR}, broad hardness ratio B_{HR}) plotted against s_Z. In every case, there is a good correlation, the width of the curves being accounted for by the uncertainties in the measured quantities. In addition there is no correlation between t_Z and s_Z or any observable quantity. This implies that s_Z tells us everything about the observable luminosity and spectrum of Sco X-1 during this observation, and that the spectral state of Sco X-1 may be described by a single parameter. Although the current observable state of Sco X-1 is well described by s_Z, s_Z cannot be used to predict (in detail) what the observable state of Sco X-1 will be in a short time (< 1 minute; see § 4.3).

From the observed broad hardness ratio B_{HR}, the state variable s_Z can be determined, as long as one knows a priori whether the source is on the normal or flaring branch. It is clear from comparison of the light curves (Figs. 2 and 3) with the spectral branch determinations (Fig. 5) that Sco X-1 was always on the flaring branch for intervals when PC mode data (data type A) was available. We fitted a straight line to the flaring branch in Fig. 7*d*, and obtained the relation

$$s_Z = 1.515 B_{HR} - 0.332 . \quad (5)$$

For PC mode data, the energy channels (1.2–5.8 keV, 5.8–15.7 keV) do not exactly match the hardness ratio energy channels (2.3–6.9 keV, 6.9–18.7 keV). By comparing PC mode data with MPC-3 mode data obtained a few minutes earlier or later, we determined a constant correction factor which we used to scale the instrumental PC mode hardness ratio into the MPC-3

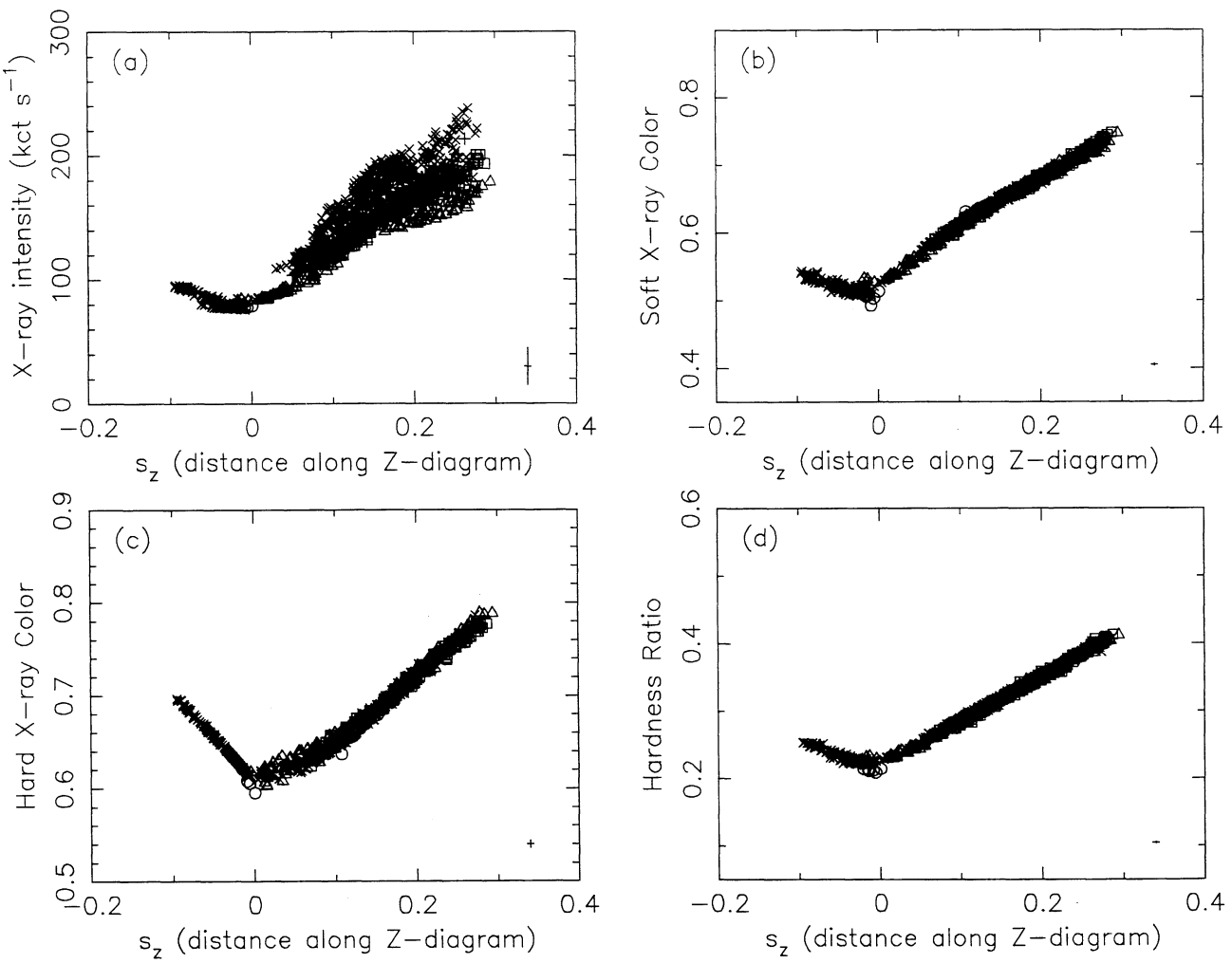

FIG. 7.—The observable characteristics of Sco X-1 are shown as a function of s_Z, the distance along the Z-diagram. Positive s_Z represents the flaring branch and negative s_Z is the normal branch. The data is binned in 32 s bins. The plotting symbols represent the various data types; a key is in Table 2. (*a*) The X-ray intensity plotted against s_Z. (*b*) The soft X-ray color S_{HR} plotted against s_Z. (*c*) The hard X-ray color H_{HR} plotted against s_Z. (*d*) The broad hardness ratio B_{HR} plotted against s_Z. Typical error bars are shown in the lower right corner.

mode hardness ratio energy channels, i.e.,

$$B_{\rm HR}({\rm PC}) = 0.58\left(\frac{\text{5.8–16.1 keV count rate}}{\text{1.2–5.8 keV count rate}}\right). \quad (6)$$

We could then determine $B_{\rm HR}$ for PC mode data using equation (6), and estimate s_z for PC mode data using equation (5).

We are now in a position to show graphically that Sco X-1 moves continuously along the Z-diagram during the campaign. In Figure 8 we show s_z, as a function of time, on an orbit by orbit basis similar to Figure 3. Note that s_z always changes continuously, which means Sco X-1 always moves along the "Z" in the color-color diagram. This behavior was previously observed for Cyg X-2 (Hasinger et al. 1990). Note also that the slope of the plot of s_z during flares, i.e., $\dot{s}_z \equiv ds_z/dt$, tends to have approximately the same magnitude (within a factor of a few). From Figures 3 and 8 we estimate that a flare takes ~ 10 minutes from beginning to end.

4.3. *Motion in the Z-Diagram*

The concept of $\dot{s}_z$ is very important if the current state of Sco X-1 is described primarily by the location of the source in the Z-diagram. In that case, s_z is a state variable, and $\dot{s}_z$ describes the past evolution of the state variable. If the future evolution of Sco X-1 could be predicted from its current state, then one would expect there to be a correlation between s_z and $\dot{s}_z$. On the other hand, the current observable properties of Sco X-1 might depend on both the source's current state (s_z) and its past state ($\dot{s}_z$), i.e., there might be physical hysteresis in the system. In this case, s_z and $\dot{s}_z$ might be independent state variables.

In Figure 9 we see that, for this observation, there is no evidence for direct correlation between s_z and $\dot{s}_z$, though there is clearly a limited region of the phase space plotted which is occupied. In particular, the spread in $\dot{s}_z$ about the axis $\dot{s}_z = 0$ is a function of s_z. From the lack of correlation, we conclude that there is no physical hysteresis in the system and that the motion of Sco X-1 in the Z-diagram, which corresponds physically to changes in intensity and spectral state, is stochastic in nature. The symmetry about $\dot{s}_z = 0$ indicates that flares are symmetric in time, i.e., a decaying flare is identical to a time-reversed rising flare. A close inspection of Figure 3 supports this observation in the time domain.

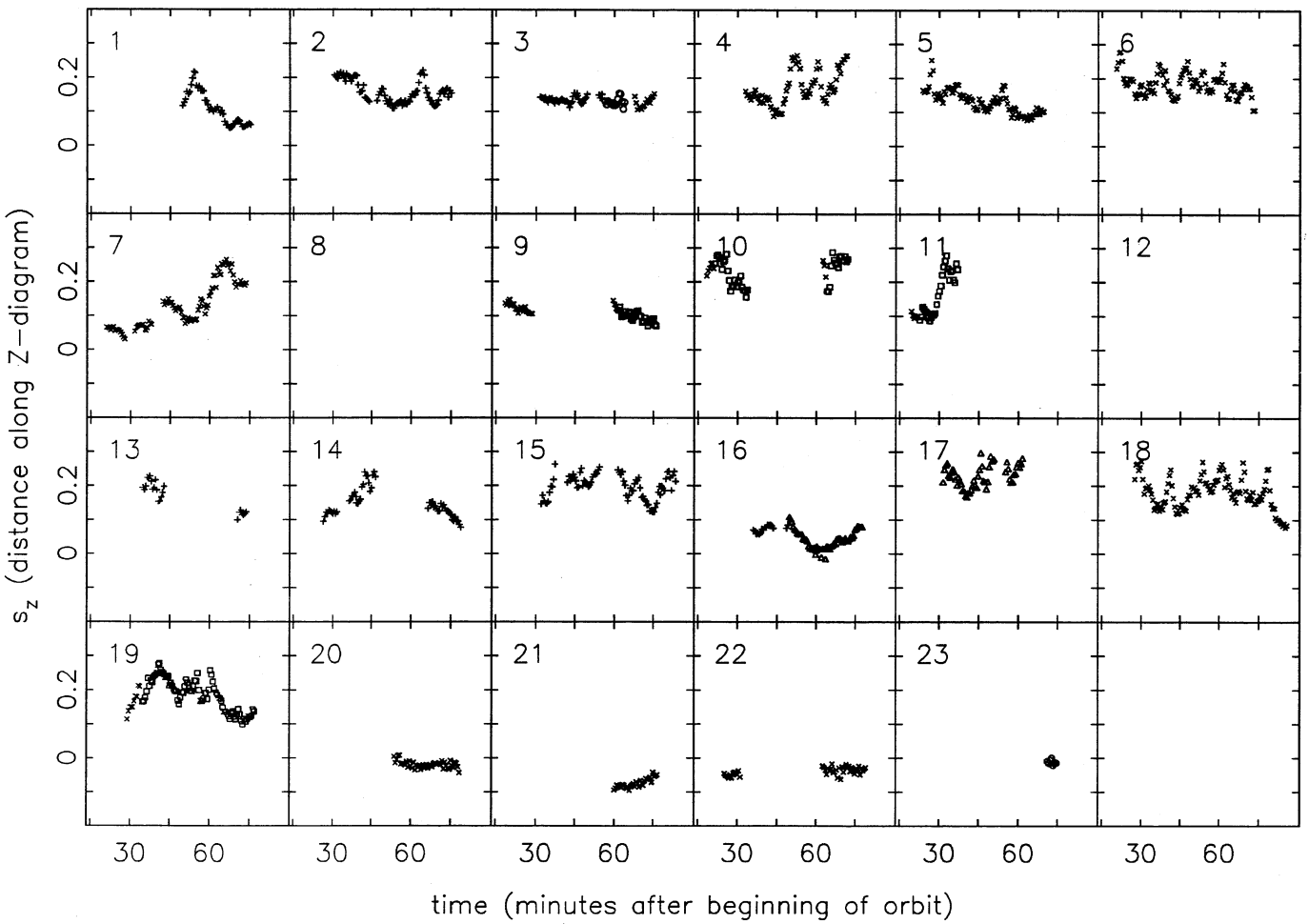

FIG. 8.—The position in the Z-diagram, s_z, plotted against time for Sco X-1 on a *Ginga* orbit-by-orbit basis. It is clear that s_z is continuous in time and that Sco X-1 moves smoothly along the Z-diagram and is never observed to jump between branches. It is also easy to see that Sco X-1 approaches the flaring branch–normal branch vertex during orbit 16 and is on the normal branch during orbits 20–23. The plotting symbols represent the various data types; a key is in Table 2. The scales are identical for each panel, and the orbit number is shown in the upper left corner of each panel. The exact times for each *Ginga* orbit are given in Table 3 and can be calculated from eq. 2.

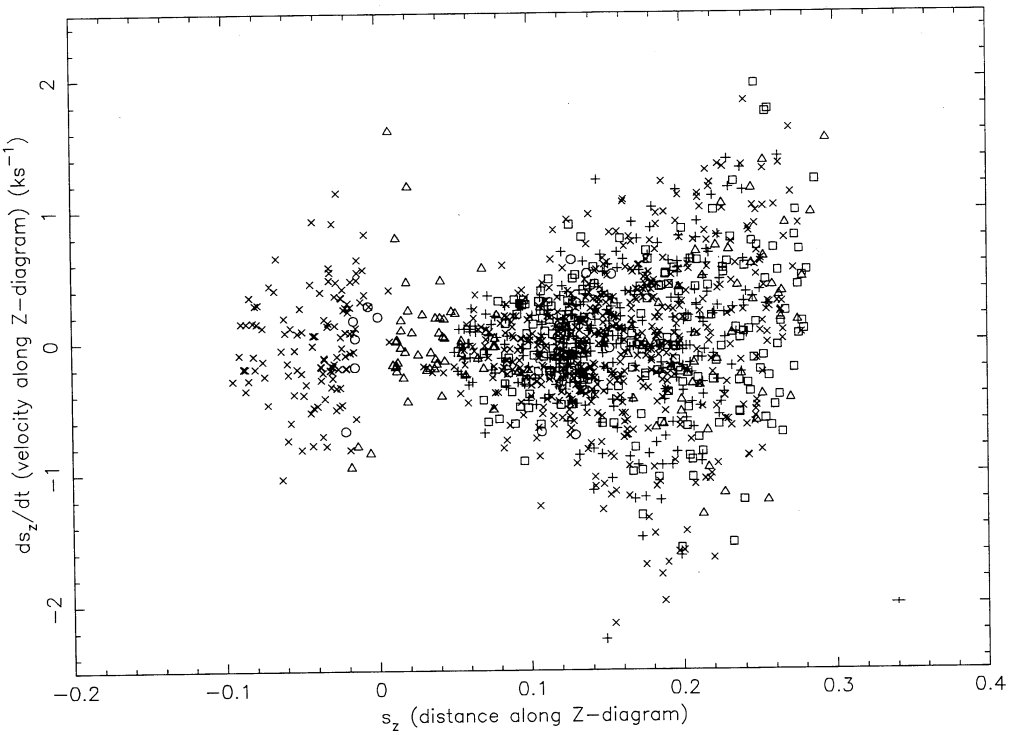

FIG. 9.—The velocity in the Z-diagram $\dot{s}_Z$ plotted against the position in the Z-diagram s_Z for Sco X-1. Note that the allowed range of velocities $\dot{s}_Z$ is a function of position s_Z. Only small velocities are observed near the flaring branch–normal branch vertex at $s_Z = 0$. Sco X-1 always moves slowly through the vertex onto the normal branch but is observed to move rapidly when it goes far out the flaring branch during a large flare. The plotting symbols represent the various data types; a key is in Table 2.

In Figure 10 we show a selection of flares in the s_Z-$\dot{s}_Z$ phase space. These flares were chosen to be well resolved from other flares and both the rise and decay of the flare were completely observed. From this figure, we can see that flares are indeed symmetrical between the rise and decay portion of their evolution. This shows as a symmetry between the top and bottom of the curves in Figure 10. We also note that all of the flares have similar shapes in the phase space trail. In the figure this is revealed by the similar ellipticity and orientation of the trails; in the time domain this would be seen as a self-similarity in flare shapes.

The populated portion of s_Z-$\dot{s}_Z$ phase space in Figure 9 is a function of s_Z. This means that the maximum speed at which Sco X-1 moves through the Z-diagram increases as Sco X-1 moves out the flaring branch, and that it always moves through the flaring branch–normal branch vertex very slowly. If instabilities in a super-Eddington accretion flow are responsible for the intensity fluctuations on the flaring branch (Lamb 1992), then we conclude that the shortest time scale for variability is a function of $\dot{M}$ and/or luminosity.

In the context of models where motion along the Z-diagram is caused by a single property of the X-ray binary, e.g., $\dot{M}$, s_Z is a function of only that property. Clearly $\dot{s}_Z$, which is a function of observable properties, is not completely correlated with s_Z. Understanding theoretically how s_Z depends on intrinsic properties of Z-sources, and what physical changes in Sco X-1 cause changes in s_Z, is a goal of current research.

5. STUDY OF QUASI-PERIODIC OSCILLATIONS AND RED NOISE

The correlation between Sco X-1's spectral state and QPO behavior has been known since the discovery of QPO in Sco X-1 (Middleditch & Priedhorsky 1986). Our observation is entirely consistent with previously observed Sco X-1 QPO behavior (see § 1). In Figure 11 we present histograms of the amount of data we have available as a function of s_Z and of data type. Recall that the flaring branch–normal branch vertex occurs at $s_Z = 0$ and that s_Z is positive on the flaring branch and negative on the normal branch. With the exception of a small amount of 8 ms types C and F data (~5 minutes), all of our high time resolution data were taken while Sco X-1 was on the flaring branch, most of it well away from the vertex ($s_Z > 0.1$). The volume and quality of our data give us the capability of studying the aperiodic and quasi-periodic processes as a function of Sco X-1's spectral state by looking for the dependence of these processes on s_Z.

5.1. *Functional Fits to Power Spectra*

Data type A, type D, and type F were used for studying the dependence of QPO, VLFN, and HFN characteristics on s_Z. Type C data were not used because there is very little (only 11 min) of that data type, and type E data were not analyzed because of its very low time resolution. The data were divided into segments with length $T = 128$ s (data type A), 256 s (data type D), or 64 s (data type F), and a fast Fourier transform (FFT) was used to determine the power spectrum for each segment. The segments were sorted by the location of Sco X-1 on the Z-diagram at the time of the data segment, and the power spectra for data of similar s_Z and identical data type were incoherently summed. The number of individual power spectra summed into each average power spectrum ranged from $N_{\rm FFT} = 7$ to 30. We have used the Leahy et al. (1983) normalization for the average power spectra and have

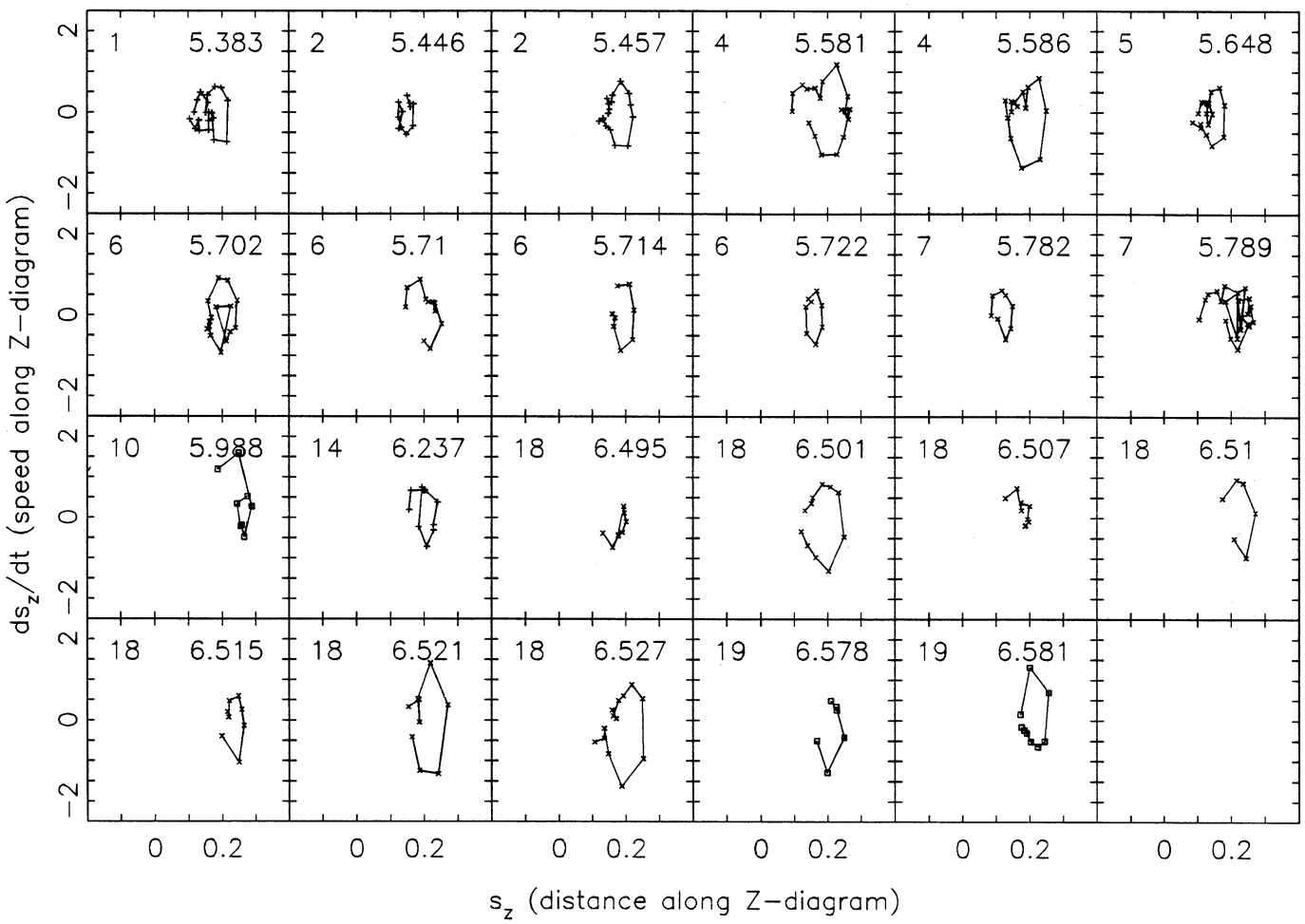

FIG. 10.—The path of Sco X-1 through s_z-$\dot{s}_z$ phase space during flares. Several well-resolved flares of various amplitudes are shown, with data points connected in time order. The self-similarity of the better resolved large flares is clear; smaller flares are probably self-similar but less well resolved in time. Each datum is a 32 s integration. Each flare is labeled with the *Ginga* orbit during which it occurred and the reduced Julian Date of the maximum intensity (see Table 3). Note that since $\dot{s}_z$ must be positive when s_z is increasing during the rising portion of a flare, Sco X-1 moves clockwise along the loop during a flare.

rebinned the average power spectra to increase signal-to-noise (see van der Klis 1989b).

The average power spectra were fitted to a model consisting of up to four components: Poisson or white noise, very low frequency noise, high-frequency noise, and quasi-periodic oscillations.

White Noise (WN).—The Poisson noise is given by a constant C_{WN}, which would be normalized to 2 in the absence of instrumental dead time effects. The high counting rates of this observation imply large dead time effects (up to 60% reduction in C_{WN}) in the LAC and this precludes their prediction. We have therefore fitted C_{WN} simultaneously with other components of the power spectra, and verified that the best-fitted value of C_{WN} is consistent with estimates (Mitsuda & Dotani 1989).

Very Low Frequency Noise (VLFN).—VLFN is a steep red noise component which dominates the lowest frequency channels in all of the Sco X-1 power spectra. It is well fitted by a power law with slope α, $f(\nu) = C_{VLFN}\,\nu^{-\alpha}$, where C_{VLFN} is the normalization. VLFN is present in observations of all Z-sources on all three spectral branches (Hasinger & van der Klis (1989).

High Frequency Noose (HFN).—HFN is a component of excess power which is observed above the steep VLFN component out to ~50 Hz. HFN was first observed on the flaring branch of Sco X-1 (Middleditch & Priedhorsky 1986), but has since been observed on all three spectral branches in Sco X-1 (Hasinger et al. 1989) and other Z-sources (Hasinger & van der Klis 1989). Previous authors have fitted HFN with an exponentially cut-off flat power law (e.g., Hasinger & van der Klis 1989); however, we obtained significantly better fits using a half-Gaussian form. The functional form used is $f(\nu) = C_{HFN}$ exp $(-\nu^2/2\sigma_{rms}^2)$, where σ_{rms} is the Gaussian rms width of the HFN and C_{HFN} is the normalization. With this functional form, the HFN drops to half its peak value at $\nu = 1.18\sigma_{rms}$.

Quasi-periodic Oscillations (QPO).—QPOs are observed on both the normal branch and the flaring branch. The shape of the QPO is well fitted by either a Lorentzian or a Gaussian. We have chosen to represent QPOs with a Lorentzian with the standard functional form $f(\nu) = C_{QPO}/[(\nu - \nu_{QPO})^2 + \gamma_{FWHM}^2/4]$, where ν_{QPO} is the QPO central frequency, γ_{FWHM} is the FWHM width of the QPO, and C_{QPO} is the normalization.

The average power spectra were fitted with WN, VLFN, and HFN and QPO when needed. The best-fit parameters were determined by minimizing, in a least-squares sense, the differences between the log of the power and the log of the fitting

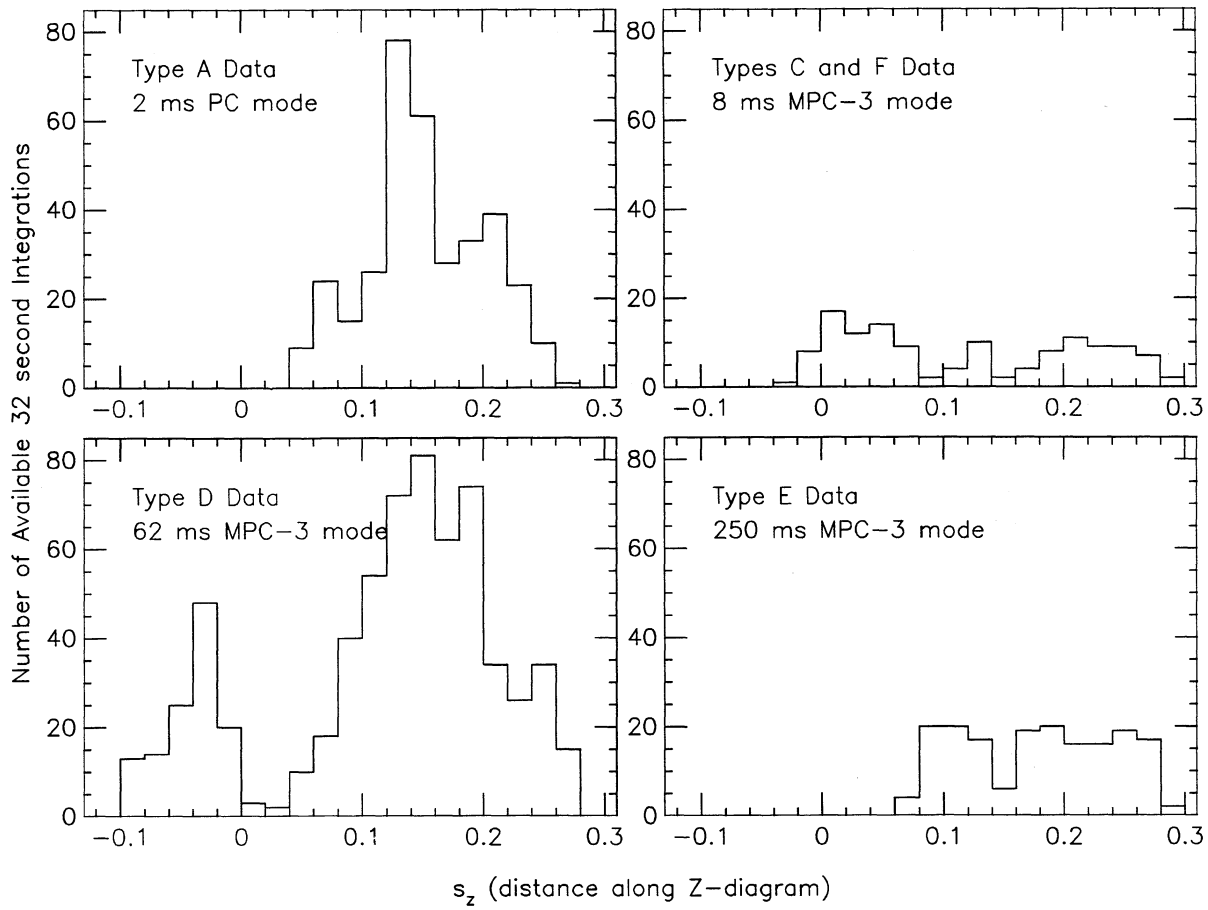

FIG. 11.—Available *Ginga* data as a function of s_Z and data type. Note that there is no high time resolution data (data type A) while Sco X-1 is on the normal branch ($s_Z < 0$), but a large amount of high time resolution data while Sco X-1 is on the flaring branch ($s_Z > 0$).

function. The results are given in Table 4. The 1 σ uncertainties are obtained by assuming that fitted parameters are independent and by determining the width of the $\chi^2_{\min} + 1$ contour projected onto the axis of interest. In addition, 95% confidence level upper limits have been estimated in several cases where HFN and QPO are not observed by fixing shape parameters at a nominal value and determining the width of the $\chi^2_{\min} + 2$ contour projected onto the axis of the normalization of the feature in question. Finally, we have estimated the fractional rms variations of the VLFN, HFN, and QPO features as a percentage of the total intensity. If A is the fractional rms variation, then van der Klis (1989b) shows that

$$A = 2\sqrt{\frac{\tau \int f(\nu) d\nu}{C_{\rm WN} N_{\rm cts}}}, \qquad (7)$$

where $N_{\rm cts}$ is the total number of counts in an average data segment, τ is the width of a data bin, and $C_{\rm WN}$ provides an empirical correction for dead time.

5.2. *Detection of Quasi-periodic Oscillations*

Because of the high detector count rate (> 10 kilocounts s^{-1}) achieved with *Ginga* on the flaring branch, we were able to detect the flaring branch QPO, which is observed only when Sco X-1 is near the vertex, $0 < s_Z < 0.025$. The observed frequency of 14.5 Hz, FWHM width of 6 Hz, and fractional rms variation of 4.9% of total intensity are all consistent with previous observations (Middleditch & Priedhorsky 1986; van der Klis et al. 1987). An average power spectrum for the period when flaring branch QPO are present is shown in Figure 12*a*. At locations further up the flaring branch ($0.025 < s_Z < 0.085$), the flaring branch QPO is not observed, with a 95% confidence upper limit to its fractional rms variation of 1.3%.

We have no high time resolution data in which we are able to see the 6 Hz normal branch QPO. However, we were able to look for normal branch QPO in the type D data, which has a time resolution of 62.5 ms. Figure 12*b* shows an average power spectrum for the normal branch data ($-0.085 < s_Z < 0$). Note the presence of normal branch QPO near the Nyquist frequency, as seen in previous observations (Middleditch & Priedhorsky 1986; Priedhorsky et al. 1986; van der Klis et al. 1987). The observed frequency of 6.3 Hz, the FWHM width of 2.1 Hz, and the fractional rms variation of 2.6% are typical. No normal branch QPO is observed in the lower flaring branch data ($0.062 < s_Z < 0.124$) with a 95% confidence upper limit fractional rms variation of 0.7%.

As discussed in § 4, we are interested in determining whether the state variable s_Z is sufficient for describing the spectral and temporal characteristics of Sco X-1, and whether there is any hysteresis in the system as indicated by dependence of properties on $\dot{s}_Z$. We know that QPO depends on s_Z, since s_Z is equivalent to location on the Z-diagram. We next searched for dependence of QPO phenomena on $\dot{s}_Z$. We separated the type F flaring branch QPO data ($0 < s_Z < 0.022$) in 32 s data seg-

TABLE 4

POWER SPECTRA COMPONENTS[a]

s_z[b]	Data Type[c]	Count Rate[d] (kilocounts s^{-1})	N_{FFT}[e]	VLFN rms[f] (%)	VLFN slope (α)	HFN rms[g] (%)	HFN σ_{rms} (Hz)	QPO rms (%)	QPO ν_{QPO} (Hz)	QPO γ_{FWHM} (Hz)
−0.085–−0.006	D	5.4	14	2.6 ± 0.1	1.82 ± 0.07			2.6 ± 0.2	6.3 ± 0.1	2.1 ± 0.4
0.062– 0.124	D	12.2	12	3.7 ± 0.2	1.65 ± 0.04			<0.7[h]		
0.132– 0.153	D	12.6	12	6.2 ± 0.2	1.82 ± 0.03					
0.154– 0.173	D	12.6	12	4.6 ± 0.2	1.67 ± 0.03					
0.179– 0.205	D	12.2	12	6.3 ± 0.2	1.76 ± 0.03					
0.209– 0.248	D	13.0	9	5.7 ± 0.3	1.65 ± 0.03					
0.055– 0.081	A	12.6	7	3.6 ± 0.3	1.79 ± 0.09	3.2 ± 0.1	13.4 ± 1.1	<0.9[h]		
0.104– 0.156	A	16.9	30	4.5 ± 0.2	1.73 ± 0.04	1.6 ± 0.1	11.6 ± 1.3			
0.163– 0.240	A	17.4	27	6.3 ± 0.3	1.72 ± 0.04	1.1 ± 0.1	4.9 ± 0.9			
−0.001– 0.022	F	7.5	10	1.9 ± 0.3	2.05 ± 0.33	2.3 ± 0.4	10.0 ± 3.2	4.9 ± 0.2	14.4 ± 0.2	6.0 ± 0.6
0.028– 0.085	F	8.2	16	2.8 ± 0.3	1.92 ± 0.17	3.0 ± 0.4	17.9 ± 3.8	<1.3[i]		
0.166– 0.278	F	13.0	23	5.4 ± 0.3	1.67 ± 0.04	<0.9[j]		<0.8[i]		

[a] See text for functional form of fitted components: power law VLFN, half-Gaussian HFN, Lorentzian QPO.
[b] Normal branch (NB): $s_z < 0$; flaring branch (FB): $s_z > 0$.
[c] Let T = duration of data segment, N = number of bins in data segment, τ = duration of data bin, fr = frequency range in power spectrum. Data type A: T = 128 s, N = 65536, τ = 2 ms, fr = 0.008–256 Hz. Data type D: T = 256 s, N = 4096, τ = 62.5 ms, fr = 0.004–8 Hz. Data type F: T = 64 s, N = 8192, τ = 7.8 ms, fr = 0.016–64 Hz.
[d] Average uncorrected detector count rate.
[e] Number of power spectra summed incoherently.
[f] Integrated over 0.005–1 Hz.
[g] Integrated over 0.01–100 Hz.
[h] 95% confidence upper limit to normal branch (NB) QPO with assumed ν_{QPO} = 6.3 Hz and γ_{FWHM} = 2.1 Hz.
[i] 95% confidence upper limit to flaring branch (FB) QPO with assumed ν_{QPO} = 14.4 Hz and γ_{FWHM} = 6.0 Hz.
[j] 95% confidence upper limit to HFN with assumed σ_{rms} = 15.75 Hz.

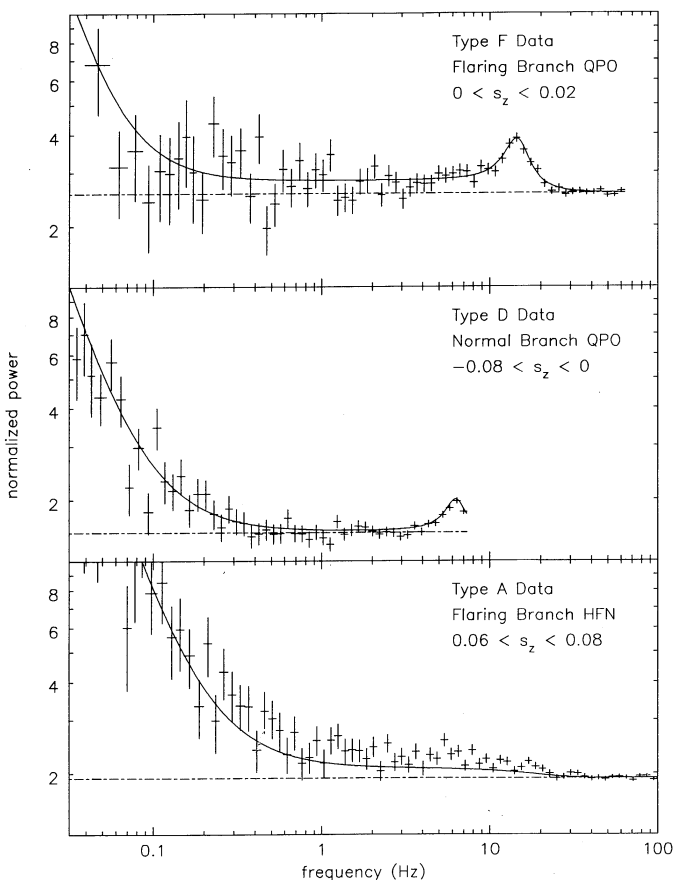

ments based on whether $\dot{s}_z$ is positive (increasing source intensity) or negative (decreasing source intensity) and calculated average power spectra for the two data sets. No statistically significant differences were found between the two average power spectra. We then sorted the data by both s_z and $\dot{s}_z$ and calculated average power spectra. For the region near the vertex in which QPO are observed, we could detect no differences between the QPO parameters for positive $\dot{s}_z$ as compared to negative $\dot{s}_z$, though it should be pointed out that we have only about 30 minutes of data in which flaring branch QPO are observed.

We observe HFN, consistent with that seen by Middleditch & Priedhorsky (1986), throughout the flaring branch (see § 5.3 below). We performed a search for QPO on the flaring branch at frequencies above the HFN cutoff of ~25 Hz. The flaring branch QPO was found in previous observations to disappear in the noise as one moved out the flaring branch (Priedhorsky et al. 1986; van der Klis et al. 1987). We created average power spectra, sorted by s_z, for type F data where no flaring branch QPO is observed ($s_z > 0.03$). We then performed searches on each of the three average power spectra which were optimized to look for signals with characteristic widths γ_{FWHM} of 1, 2, and 4 Hz. No significant excesses above the Poisson level (corrected for dead time) were found. Upper limits on fractional rms variations are given in Table 5. The upper limits to these QPO, as well as for the coherent pulsations descibed in §§ 6.1 and 6.2,

FIG. 12.—Average power spectra for Sco X-1. Three average power spectra show the VLFN, HFN, and QPO components. The solid line shows the best-fitted model, and the dashed-dotted line shows the fitted Poisson noise level. Parameters of the fitted models are given in Table 4. (*a*) Type F data showing the flaring branch QPO; HFN is clearly visible between 0.5 and 5 Hz. (*b*) Type D data showing the normal branch QPO. (*c*) Type A data showing HFN between 1 and 20 Hz.

TABLE 5

LIMITS ON rms AMPLITUDE FOR QUASI-PERIODIC OSCILLATIONS ON THE FLARING BRANCH AT FREQUENCIES ABOVE 25 HERTZ[a]

	rms LIMITS AT ν_{QPO} = 32 Hz			rms LIMITS AT ν_{QPO} = 55 Hz		
s_Z RANGE	1 Hz[b]	2 Hz[b]	4 Hz[b]	1 Hz[b]	2 Hz[b]	4 Hz[b]
0.03–0.12.....	1.35%	1.61%	1.91%	1.68%	2.00%	2.37%
0.12–0.21.....	0.92%	1.10%	1.31%	1.15%	1.37%	1.63%
0.21–0.30.....	1.19%	1.42%	1.68%	1.48%	1.77%	2.09%

[a] 99% confidence level.
[b] Assumed width γ_{FWHM} of QPO in search.

were determined using the methods of van der Klis (1989b). In determining the number of independent frequency channels we counted the total number of channels searched in all three power spectra and for all three characteristic frequency widths. The 99% confidence level upper limits quoted thus represent the probability that no excess power is present at any of the three characteristic frequency widths in any of the three power spectra covering the upper flaring branch ($s_Z > 0.03$).

5.3. *Dependence of Noise Characteristics on s_Z*

A second aspect of temporal variability is the red noise. We have investigated the dependence of the flaring and normal branch VLFN ($\nu < 1$ Hz) and flaring branch HFN (1 Hz $< \nu <$ 50 Hz) on both s_Z and $\dot{s}_Z$. The large amount of high time resolution *Ginga* data obtained while Sco X-1 was on the flaring branch allows us to characterize changes in VLFN and HFN as Sco X-1 moves out the flaring branch.

VLFN has been previously observed in Sco X-1 on all branches of the Z-diagram, and we detect it in all of our average power spectra. In Figure 13 we show the changes in α, the VLFN power-law index, and in the fractional rms variation of the VLFN as Sco X-1 moves out the flaring branch by plotting these measured quantities as a function of s_Z. It has been previously noted that the fractional rms variation of VLFN is larger on the flaring branch than on the normal branch. Middleditch & Priedhorsky (1986) and Hasinger & van der Klis (1989) both observe fractional rms variations of $\sim$2.5% on the normal branch and $\sim$6% on the flaring branch. In Figure 13*a*, we see that the fractional rms variations of VLFN change smoothly from 2% at the normal branch–flaring branch vertex to 6% at the upper end of the flaring branch. The VLFN power-law index α, however, was found to be independent of s_Z on the flaring branch, $\alpha = 1.72 \pm 0.01$ (Fig. 13*b*). This supersedes the contrary preliminary results of Hertz et al. (1990b).

HFN has also been observed on all three branches of the Z-diagram for Sco X-1 (Hasinger et al. 1989). Hasinger & van der Klis (1989) found similar amounts of HFN on both the normal and flaring branches, with a fractional rms variation of $\sim$4.5% and an exponential cutoff of $\sim$58 Hz. As previously noted, we obtained better fits to HFN with a half-Gaussian than with an exponentially cutoff power law. In Figure 14 we show that both the fractional rms variation and the Gaussian width of the HFN change as Sco X-1 moves out the flaring branch. The fractional rms variation decreases from 3% near the normal branch–flaring branch vertex to $\lesssim$1% at the upper end of the flaring branch. There is also evidence for the HFN to become less broad as s_Z increases (Fig. 14*b*); however, this conclusion rests principally on the single measurement of HFN

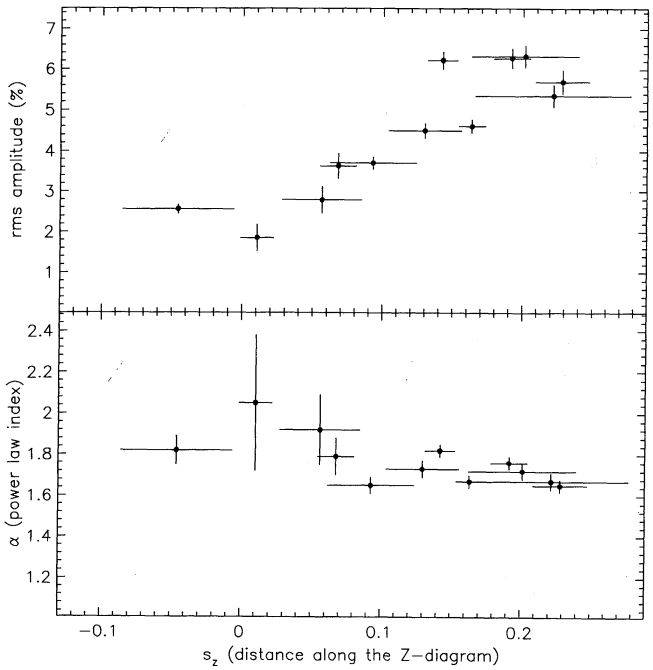

FIG. 13.—Characteristics of normal and flaring branch VLFN as a function of s_Z. For $s_Z < 0$ the source is on the normal branch, and for $s_Z > 0$ the source is on the flaring branch. Over the flaring branch, the power-law index α remains constant and the fractional rms variation increases threefold. During this same time, the source exhibits intensity variations of over 50%. Data are from Table 4.

at $s_Z = 0.2$. The disagreement in our amplitudes with those of Hasinger & van der Klis (1989) indicates that there may be problems in separating HFN from other components in the power spectra. The power spectra in Figure 12 show that HFN is an unambiguous component of Sco X-1's power spectra.

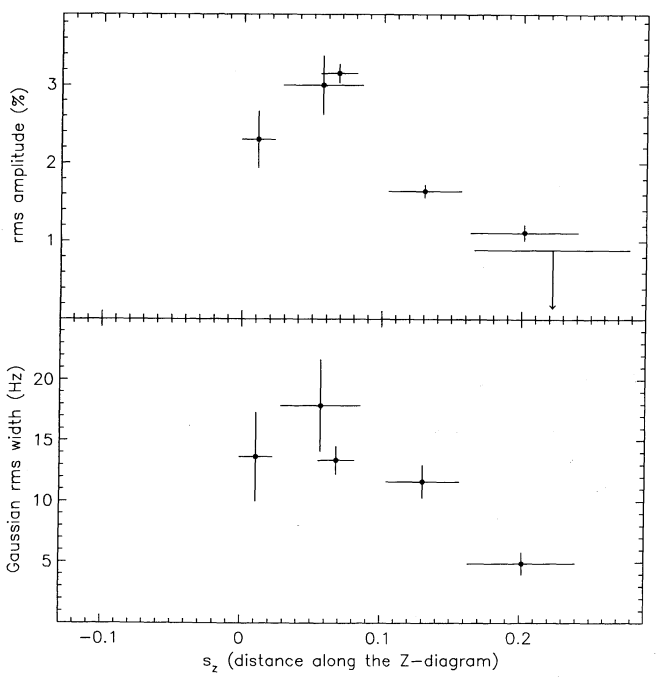

FIG. 14.—Characteristics of flaring branch HFN as a function of s_Z. A clear decrease in the fractional rms variation is seen along the flaring branch, and there is evidence for a decrease in the width of the HFN component as well. Data are from Table 4.

TABLE 6

ENERGY-DEPENDENT POWER SPECTRA COMPONENTS[a,b]

s_Z	Energy Channel[c]	Count Rate[d] (kilocounts s^{-1})	N_{FFT}[e]	VLFN rms[f] (%)	VLFN slope (α)	HFN rms[g] (%)	HFN σ_{rms} (Hz)
0.055–0.081.....	Low	8.7	7	3.0 ± 0.3	1.80 ± 0.11	2.5 ± 0.2	14.2 ± 2.6
0.104–0.156.....	Low	11.1	30	3.6 ± 0.1	1.67 ± 0.04	1.5 ± 0.2	15.0 ± 3.3
0.163–0.240.....	Low	10.9	27	4.9 ± 0.2	1.68 ± 0.04	1.0 ± 0.2	7.6 ± 2.8
0.055–0.081.....	High	3.9	7	5.6 ± 0.6	1.97 ± 0.12	5.4 ± 0.3	17.5 ± 1.9
0.104–0.156.....	High	5.8	30	6.4 ± 0.2	1.72 ± 0.04	2.4 ± 0.2	12.3 ± 1.8
0.163–0.240.....	High	6.5	27	9.0 ± 0.3	1.79 ± 0.03	1.6 ± 0.1	4.9 ± 1.0

[a] See text for functional form of fitted components: power-law VLFN, half-Gaussian HFN, Lorentzian QPO.
[b] Data type A: $T = 128$ s, $N = 65536$, $\tau = 2$ ms, fr = 0.008–256 Hz.
[c] Low channel: 1.2–5.8 keV; high channel: 5.8–15.7 keV.
[d] Average uncorrected detector count rate.
[e] Number of power spectra summed incoherently.
[f] Integrated over 0.005–1 Hz.
[g] Integrated over 0.01–100 Hz.

We have also detected energy-dependent characteristics in the VLFN and HFN components of Sco X-1's variability. Power spectra have been determined separately for both the low- and high-energy channels of the type A data in exactly the same manner as they were for the total count rate. The low-energy channel covers 1.2–5.8 keV and the high-energy channel covers 5.8–15.7 keV. In Table 6 we show the results of fits to power spectra from both channels as a function of s_Z. We note several significant results. The trends in fitted parameters (C_{VLFN}, C_{HFN}, σ_{rms}) as a function of s_Z are clearly present in both channels. The VLFN power-law index α is consistent with the previously determined mean value in all cases. Both noise components (VLFN and HFN) have higher fractional rms variations in the high-energy channel than in the low-energy channel, with $A_{high} \simeq 2A_{low}$. Within the statistical uncertainties, the Gaussian width of the HFN is the same in both channels.

For a final check, we summed all of the type F upper flaring branch power spectra ($s_Z > 0.03$) into two average power spectra which were sorted by the sign of $\dot{s}_Z$. There is no difference in either VLFN or HFN between power spectra obtained when $\dot{s}_Z > 0$ and $\dot{s}_Z < 0$. Once again, no evidence was found for any hysteresis in the observable characteristics of Sco X-1.

6. SEARCH FOR MILLISECOND PULSATIONS

The *Ginga* observations are well suited for searching for coherent short time scale phenomena, such as millisecond pulsations, in addition to QPO. The PC mode data (data type A) has 1 ms time resolution, and the high bit rate MPC-3 data (data types C and F) has a time resolution of 8 ms. In addition, 3.4 hr of unfiltered optical data with 10 ms time resolution was obtained by K. Horne and E. Robinson at McDonald Observatory overlapping 4 minutes of *Ginga* observations. We have systematically searched both the X-ray and high time resolution optical data for evidence of rapid coherent pulsations.

6.1. *Coherent X-Ray Pulsations*

There are several reasons to search for short-period, coherent X-ray pulsations from Sco X-1 and other LMXBs. These include the hypothesis that millisecond period radio pulsars evolve from LMXBs, which must necessarily have rapidly rotating neutron star primaries (Alpar et al. 1982), and the requirements of the beat frequency modulated accretion model for X-ray QPOs, where the QPO frequency is the beat frequency between the rotation of the neutron star and the Keplerian orbital frequency at the Alfvén radius (Lamb et al. 1985). Both models require LMXBs, in particular Z-sources, to have neutron star spin periods in the 1–20 ms range. If the neutron star is magnetized, as it must be in both cases, then coherent X-ray pulsations are expected (see Wood et al. 1991 for a complete discussion).

We have conducted a thorough search of the *Ginga* data for X-ray pulsations from Sco X-1. For the short pulse periods searched (down to 2 ms) and the long continuous data integrations used (up to 35 minutes), there is significant Doppler smearing of the X-ray pulsations due to the 19.2 hr orbital period of Sco X-1. At the highest frequency resolution, this can amount to spreading the signal over ~ 56 channels in the power spectrum (Wood et al. 1991). Since the orbital modulation of Sco X-1 has never been observed in X-ray data, the phase of the Doppler shift of any X-ray pulsations is unknown. In addition, the orbital period and Doppler amplitude are not known precisely enoughto correct millisecond time resolution data a priori.

We have therefore used the coherence recovery technique of Wood et al. (1991) to correct for the unknown amount of Doppler smearing. With this method, the unknown orbit is approximated by a one-parameter family of parabolas. The data are transfomed to the parabolic orbit using a quadratic time transformation. For the correct parabola and for sufficiently short integration periods, the Fourier transform of the quadratically time-transformed data will contain all of the pulsed signal at a single frequency. For details on the technique, its implementation, and its limitations, see Hertz et al. (1990a) and Wood et al. (1991).

We divided the seven orbits of high time resolution *Ginga* data (data type A) into nine segments of continuous data. The segments ranged in length from 2 minutes (2^{17} bins of duration 0.98 ms) to 34 minutes (2^{21} bins). To implement the coherence recovery technique, the quadratic parameter α of Wood et al. is varied between $-\alpha_{max}$ and $+\alpha_{max}$ with a resolution of $\delta\alpha$. For the period of Sco X-1 and the resolution and duration of the *Ginga* observations, $\alpha_{max} = 5 \times 10^{-9}\ s^{-1}$ and $\delta\alpha = 10^{-10}\ s^{-1}$.

No coherent pulsations are detected at the 95% confidence level with pulse fractions exceeding 0.19% for $\nu < 50$ Hz and

0.26% for $\nu < 400$ Hz. In particular, no evidence is found for pulsations at periods between 2.83 ms and 3.03 ms with a 95% confidence level upper limit to the pulse fraction of 0.14% for any such pulsations (cf. Leahy 1987). A previous search through *EXOSAT* data by Middleditch & Priedhorsky (1986), also incorporating corrections for Doppler smearing, yielded 90% confidence limits for the pulse fraction of 0.5% for $\nu < 125$ Hz and 0.8% for $\nu < 250$ Hz.

6.2. *Optical Quasi-Periodic Oscillations and Coherent Pulsations*

V818 Sco, the optical counterpart of Sco X-1, was observed during the campaign with the 36 inch (91 cm) telescope at McDonald Observatory by E. Robinson and K. Horne. High time resolution optical data, with 10 ms time resolution, were obtained in unfiltered white light. Although observations were planned for both nights of the campaign, technical problems prevented observations on the first night. On the second night, 1991 March 11, 3.4 hr of data were obtained, between 8:24 and 11:50 UT. This time period includes orbit 23 of *Ginga* observations, during which 4 minutes of type C data were obtained.

Data were obtained simultaneously from a comparison/guide star located near V818 Sco. The average signals were 8845 counts s^{-1} from V818 Sco and 51060 counts s^{-1} from the comparison star. We assume that the comparison star was not varying during the observations, and interpret the slow increase in both the comparison star and V818 Sco as due to changing air mass. After cleaning the data for dropouts due to guide checks and for noise spikes which occurred when either the dome or telescope was moved, we binned the comparison star data in 1 s bins and fitted a fourth order polynomial to the comparison star data. Finally we divided the V818 Sco data by that curve to yield our high time resolution optical data set.

We searched for both periodic and quasi-Periodic signals in the data by performing FFTs of the data and calculating the power spectrum. Power spectra with 50 Hz resolution were determined for (i) the entire 3.4 hr observation, (ii) incoherent summation of 2408 power spectra, each of which corresponds to 5.12 s of data, and (iii) the incoherent summation of 64 power spectra, each of which contains 5.12 s of data, obtained during the 4 minutes of data for which there are simultaneous X-ray data.

In none of the power spectra is there any significant coherent or incoherent signal, with the exception of an increase in noise at low frequency. This red noise is present in power spectra of the comparison star as well and can be attributed to systematic uncertainties in the extinction correction as well as guiding errors during the observation. We do not believe it is related to the LFN observed in X-ray spectra of Sco X-1. From the single coherent power spectrum, we set a 95% confidence level upper limit to the pulse fraction of coherent pulsations of 0.10% for $\nu < 50$ Hz. No evidence for optical quasi-Periodic oscillations are seen in the incoherently summed spectra and we set a 95% confidence level upper limit of 0.23% of intensity to the fractional rms variation of any QPO with $\nu < 50$ Hz.

We cross-correlated the 200 s of X-ray data from *Ginga* orbit 23 with simultaneous optical photometry. Since the X-ray data are sampled at 8 ms and the optical data are sampled at 10 ms, we performed the cross-correlation with 10 ms bins and took whichever X-ray time bin was nearest to the time lagged optical time bin. We calculated cross-correlation amplitudes for time lags out to 10 s, with 10 ms resolution. No significant signal was seen at the 95% confidence level. This is expected since the optical signal is produced primarily through reprocessing of X-rays in the accretion disk, and the X-ray signal is broadened by the ~ 1 s light crossing time for the inner accretion disk. This is more than enough to smear a high-frequency X-ray signal, for instance, the 15 Hz flaring branch QPO.

7. DISCUSSION

We have begun the process of looking for observable changes in the spectral and temporal characteristics of Sco X-1 as it changes its spectral and intensity properties and moves along the Z-diagram. As a start to this task we have defined s_Z, a parameter which describes the source's position in the Z-diagram; as we have noted, the exact value of s_Z depends on the detector response and on the choice of energy channels used to create the Z-diagram. According to the unified model discussed by Lamb (1989, 1992), the state of the source is described by a single parameter, usually thought to be the mass accretion rate $\dot{M}$. $\dot{M}$ is not observable, but we might expect a single function of observable parameters to characterize the source state.

We have shown that all observable spectral and temporal characteristics can be predicted from the value of s_Z. In particular we see that intensity, spectral hardness, QPO frequency and fractional variation, VLFN index and fractional variation, and HFN width and fractional variation can all be unambiguously determined from s_Z. In the context of the unified model, this would imply that s_Z is a function only of $\dot{M}$ and that s_Z can be used to characterize the system behavior.

We then looked for evidence of hysteresis in the system by looking for correlations between observable quantities (e.g., hardness, QPO frequency, VLFN index) and the history of the source. The past behavior can be quantified by determining $\dot{s}_Z$, the rate of change of position in the Z-diagram. We found no correlations or dependencies for observable quantities. However, we found that the source is constrained in the rate at which it can move through the Z-diagram by its current location on the Z-diagram. In particular, we found that the source always moves slowly from the flaring branch through the vertex to the normal branch ($|\dot{s}_Z| < 0.4 \times 10^{-3}$ s^{-1}), yet the source moved rapidly during the large flares which send the source out along the flaring branch ($|\dot{s}_Z| \simeq 1$–1.4×10^{-3} s^{-1}).

This behavior constrains physical models of Sco X-1 on the flaring branch. In the unified model, the flaring behavior occurs when overstable photohydrodynamic modes excite instabilities in the super-Eddington flow (Fortner, Lamb, & Miller 1989). This segregates the matter, allowing continued accretion and large increases in luminosity, despite the accretion rate exceeding the Eddington limit, as well as reducing the average optical depth seen by the radiation and causing the correlated spectral changes. Although the models of Fortner et al. (1989) have successfully accounted for the observed 10–20 Hz flaring branch QPO frequency, the question of the rate of change in $\dot{M}$ as a function of $\dot{M}$ has not been explored. Our observations provide constraints on the available rates of change of accretion rates for these models, which assume a strong correlation between $\dot{M}$ and luminosity on the flaring branch.

We would like to thank the members of the *Ginga* team, in particular F. Makino, for undertaking the difficult and potentially hazardous observation of Sco X-1. B. Vaughan and K. S. Wood would also like to thank the *Ginga* team for their hospi-

tality during and after the observation. We thank K. Horne and E. Robinson for obtaining the high time resolution optical observations of V818 Sco during the multiwavelength campaign. The Sco X-1 multiwavelength campaign grew out of discussions between some of the authors and other participants, in particular W. Penninx and W. H. G. Lewin, at the 1988 Los Alamos Workshop on Quasi-Periodic Oscillations. This work is supported by grants from the National Aeronautics and Space Administration to the Naval Research Laboratory and Stanford University under the *Ginga* Visiting Guest Investigator Program. P. Hertz and K. S. Wood acknowledge partial support by the Office of Naval Research. B. Vaughan was supported in part by the Netherlands Organization for Scientific Research under grant PGS 78-277.

REFERENCES

Alpar, M. A., Cheng, A. F., Ruderman, M. A., & Shaham, J. 1982, Nature, 300, 728
Augesteijn, T., et al. 1992, A&A, submitted
Bradt, H. V., et al. 1975, ApJ, 197, 443
Canizares, C. R., Clark, G. W., Lewin, W. H. G., Schnopper, H. W., Sprott, G. F., Hjellming, R. M., & Wade, C. M. 1973, ApJ, 179, L1
Canizares, C. R., et al. 1975, ApJ, 197, 457
Dotani, T., & Mitsuda, K. 1988, in Physics of Neutron Stars and Black Holes, ed. Y. Tanaka (Tokyo: Universal Academy Press), 143
Fortner, B., Lamb, F. K., & Miller, G. S. 1989, Nature, 342, 775
Hasinger, G. 1987, A&A, 186, 153
———. 1988a, in Physics of Neutron Stars and Black Holes, ed. Y. Tanaka (Tokyo: Universal Academy Press), 97
———. 1988b, Adv. Space Res., 8, 377
Hasinger, G., Priedhorsky, W., & Middleditch, J. 1989, ApJ, 337, 843
Hasinger, G., & van der Klis, M. 1989, A&A, 225, 79
Hasinger, G., van der Klis, N., Ebisawa, K., Dotani, T., & Mitsuda, K. 1990, A&A, 235, 131
Hertz, P., Norris, J. P., Wood, K. S., Vaughan, B. A., & Michelson, P. F. 1990a, ApJ, 354, 267
Hertz, P., Norris, J. P., Wood, K. S., Vaughan, B. A., Michelson, P. F., Mitsuda, K., & Dotani, T. 1990b, in Accretion Powered Compact Binaries, ed. C. W. Mauche (Cambridge: Cambridge Univ. Press), 43
Hertz, P., Wood, K. S., Norris, J. P., Vaughan, B. A., Michelson, P. F., Mitsuda, K., & Dotani, T. 1992, in Frontiers of X-ray Astronomy, ed. Y. Tanaka & K. Koyama (Tokyo: Universal Academy Press), in press
Hjellming, R. M., Han, X. H., Córdova, F. A., & Hasinger, G. 1990a, A&A, 235, 147
Hjellming, R. M., et al. 1990b, ApJ, 365, 681
Ilovaisky, S. A., Chevalier, C., White, N. E., Mason, K. O., Sanford, P. W., Delvaille, J. P., & Schnopper, H. W. 1980, MNRAS, 191, 81
Lamb, F. K. 1989, in Proc. 23rd ESLAB Symposium on Two Topics in X-Ray Astronomy, ed. J. Hunt & B. Battrick (ESA SP-296), 215
———. 1992, in Neutron Stars, ed. J. Ventura (Dordrecht: Kluwer), in press
Lamb, F. K., Shibazaki, N., Shaham, J., & Alpar, M. A. 1985, Nature, 317, 681
Langmeier, A. 1988, Ph.D. thesis, Universität München, MPE Report 210.
Leahy, D. A. 1987, IAU Circ., 4485
Leahy, D. A., Darbro, W., Elsner, R. F., Weisskopf, M. C., Sutherland, P. G., Kahn, S., & Grindlay, J. E. 1983, ApJ, 266, 160
Lewin, W. H. G., & Joss, P. C. 1983, in Accretion Driven Stellar X-ray Sources, ed. W. H. G. Lewin & E. P. J. van den Heuvel (Cambridge: Cambridge Univ. Press), 41
Lewin, W. H. G., van Paradijs, J., & van der Klis, M. 1988, Space Sci. Rev., 46, 273
Maisack, M., et al. 1992, in preparation
Makino, M. 1987, Astrophys. Lett. Comm., 25, 223
Mason, K. O. 1988, in Multiwavelength Astrophysics, ed. F. Córdova (Cambridge: Cambridge Univ. Press), 133
Middleditch, J., & Priedhorsky, W. 1986, ApJ, 306, 230
Mitsuda, K., & Dotani, T. 1989, PASJ, 41, 557
Miyamoto, S., & Matsuoka, M. 1977, Space Sci. Rev., 20, 687
Mook, D. E., et al. 1975, ApJ, 197, 425
Pan, H. C., et al. 1992, in preparation
Penninx, W., Lewin, W. H. G., Zijlstra, A. A., Mitsuda, K., van Paradijs, J., & van der Klis, M. 1988, Nature, 366, 146
Penninx, W., Lewin, W. H. G., Mitsuda, K., van Paradijs, J., van der Klis, M., & Zijlstra, A. A. 1990, MNRAS, 243, 114
Petro, L. D., Bradt, H. V., Kelley, R. L., Horne, K., & Gomer, R. 1981, ApJ, 251, L7
Priedhorsky, W., Hasinger, G., Lewin, W. H. G., Middleditch, J., Parmar, A., Stella, L., & White, N. E. 1986, ApJ, 306, L91
Turner, M. J. L., et al. 1989, PASP, 41, 345
van der Klis, M. 1989a, ARA&A, 27, 517
———. 1989b, in Timing Neutron Stars, ed. H. Ogleman., & E. P. J. van den Heuvel (Dordrecht: Kluwer), 27
van der Klis, M., Stella, L., White, N., Jansen, F., & Parmar, A. N. 1987, ApJ, 316, 411
van Paradijs, J., et al. 1990, A&A, 235, 156
Vrtilek, S. D., Raymond, J. C., Garcia, M. R., Verbunt, F., Hasinger, G., & Kürster, M. 1990, A&A, 235, 162
Vrtilek, S. D., Penninx, W., Raymond, J. C., Verbunt, F., Hertz, P., Wood, K., Lewin, W. H. G., & Mitsuda, K. 1991, ApJ, 376, 278
White, N. E. 1989, A&AR, 1, 85
Willis, A. J., et al. 1980, ApJ, 237, 596
Wood, K. S., Hertz, P., Norris, J. P., Vaughan, B. A., Michelson, P. F., Mitsuda, K., & Dotani, T. 1989a, in Proc. 23rd ESLAB Symp. on Two Topics in X-Ray Astronomy, ed. J. Hunt & B. Battrick (ESA SP-296), 557
———. 1989b, BAAS, 21, 1206
Wood, K. S., et al. 1991, ApJ, 379, 295